World-to-digital microfluidics for transformation and enzymatic assays

Ehsan Moazami

A Thesis

In the Department

of

Electrical and Computer Engineering

Presented in Partial Fulfillment of the Requirements

For the Degree of

Master of Applied Science (Electrical and Computer Engineering) at

Concordia University

Montreal, Quebec, Canada

December 2018

Abstract

World-to-digital microfluidics interfaces for transformation and enzymatic assays

Ehsan Moazami

Digital microfluidics (DMF) is a technique for the manipulation of discrete droplets on an array of electrodes, which allows the controlled movement of fluids and represents an alternative from the conventional microfluidic paradigm of transporting fluids in enclosed channels. One of the major benefits of DMF is that fluid motion and control is achieved without external pumps and fabricated valves – it only requires the use of electric fields. The automation component of DMF has pushed the barriers of this 'lab-on-chip' technology; however, integration with external components (i.e. world-to-chip) interfaces has been a challenge. For example, the delivering of the biological fluids to the chip and integrating temperature control on a single platform are considered as two world-to-chip challenges in DMF. To address these two challenges, my thesis describes two world-to-chip components that are integrated with the DMF device: reagent delivery and temperature control. This new platform enables us to perform a variety of biological or chemical experiments on a chip with reduced manual intervention. Specifically, the new platform enabled an increase in reservoir volume on the chip by 40-fold from ~10 µL to 400 µL which allowed more reproducible dispensing and eliminated the need to refill the reservoirs during the biological assay. In addition, we integrated a closed-loop temperature control system that enabled fast and rapid changes in temperature on the chip.

To show the utility of the world-to-chip interfaces, we validated the system by automating bacterial transformation and enzymatic assay procedures, which show that both procedures require world-to-chip interfaces for accurate and precise implementation. Overall, we propose that this system has the potential to be integrated for other types of biological assays and experiments which require fluidic control, automation, and temperature control.

Acknowledgements

First and foremost, I would like to thank my supervisor, Dr. Steve Shih for agreeing to take me onboard this crazy journey and empowering me to express my scientific curiosity. His enthusiasm and inexhaustible motivation inspired me to become the graduate student that I am today. In addition, his interdisciplinary vision of science pushed me to see beyond my preconceptions of the research world.

Next, I would like to thank my entire lab for their help and support throughout these past two years. Their value in my project cannot be underlined enough. Special mention to James Perry and Mathieu Husser for their tremendous help in biology part. Their science knowledge was an important part of this project and I learned a lot from them. Another special thanks to Guy Soffer for his great simulation and programming experience who offered me a great help towards simulation. Great thanks to Kenza Samlali for all her kind assistance. Her mix of straightforward criticism combined with heart-warming support have always given me great confidence and a better insight into my research experience. Thank you to Philippe Vo and Mathieu Husser for their great work as exemplary undergrads.

I thank the ECE department for their FRS funding and for curating such a pleasant master's program. I recognize the entire Martin Lab for their constant good will and for providing me with the scientific advice I was lacking. I also thank the Martin Lab and the Centre for Applied Synthetic Biology for their resources and making the working environment so pleasant. Thank you to the Sacher Lab for their help with tissue culturing.

Next, I thank my committee members, Dr. Wahab Hamou-Lhadj (who is also acting as chair) and Dr. Sana Jahanshahi-Anbuhi, for reading, reviewing and providing comments for my thesis.

I thank my parents for respecting my decisions and giving me the keys to success and caring and sacrifices you have done for educating and preparing me for my future. Thank you, mother, for your everyday prayers for me.

My acknowledgement would be incomplete without thanking my adorable wife, Maryam. Words fail to express how grateful I am to you, whose love and support has been the biggest source of my strength. Thank you for believing in me and for inspiring me to follow my dreams. This would not have been possible without your unwavering and unselfish love and support given to me at all times. And great thanks to my newborn son, Ryan, who made me laugh all the time and gave me bright sign of hope and freshness.

Overview of Chapters

This thesis describes the project I conducted and completed for my Master's in Applied Science in Dr. Steve Shih's research group at Concordia University. In this work, I aimed to develop a new world-to-chip interface prototype for digital microfluidic platform tailored to integrate reagent delivery system and temperature control system simultaneously on a chip. This thesis provides a literature review on the history of miniaturization and microfluidic paradigms, an in-depth review of digital microfluidics and a commentary on the state of world-to-chip techniques while assessing the technological challenges in operating world-to-chip interface. I will then get into the core of my research, reporting the methodology utilized for the development of a world-to-digital microfluidics platform, and validating the platform with biological assays.

Chapter 1 is an introduction to microfluidics within the larger realm of miniaturization, describing the three dominant paradigms and briefly evaluating their potential for cell-based applications. From this review, we will draw a table comparing the three paradigms.

Chapter 2 provides an in-depth review of digital microfluidics theory, venting its merits as a versatile liquid handling platform, describes the fabrication methods, assess the potential for automation and finally comments on its current state in relation to world-to-chip interfaces.

Chapter 3 is a review presenting the current world-to-chip interfacing techniques with a special focus on reagent delivery system and temperature control on DMF chips, and comments on the technological limitations in operating world-to-chip interface today. This commentary will lead to the **presentation of my thesis objectives**.

Chapter 4 provides a complete description of my biological and engineering methods. Specifically, I describe the development of a functional world-to-chip interface for digital microfluidics. In addition, I describe how to integrate two different world-to-chip systems on a

digital microfluidic platform. These interfaces include 1) a reagent delivery system and 2) a closed-loop temperature control system.

Chapter 5 describes my results in validating the world-to-chip interfaces. I will describe the optimization of device design and the results pertaining to validating the platform for two biological applications, namely bacterial transformation and enzymatic assay.

Chapter 6 provides concluding remarks regarding my work and its potential in clinical research. I will also evaluate future perspectives for my platform in relation to world-to-chip interfaces.

Appendix provides additional information regarding our experiments. This includes a table showing the strains and plasmids used in this thesis, a series of images showing the fluidic operation of the device for dispensing and for the assays, and a description of the Simulink block diagrams for the thermoelectric module and thermal plant.

Table of Contents

List of Figures

List of Tables

List of Equations

List of Abbreviations

1. Alternating Current (**AC**)
2. Digital Microfluidics (**DMF**)
3. Optical Density (**OD**)
4. Lab-on-a-chip (**LOC**)
5. Reynolds Number (**Re**)
6. Polydimethylsiloxane (**PDMS**)
7. Dielectrophoresis (**DEP**)
8. Computer-Aided Design (**CAD**)
9. Deoxyribonucleic Acid (**DNA**)
10. Indium Tin Oxide (**ITO**)
11. Electrowetting-on-Dielectric (**EWOD**)
12. Graphical user interface (**GUI**)
13. Printed Circuit Board (**PCB**)
14. Deionized (**DI**)
15. Isopropanol (**IPA**)
16. Direct Current (**DC**)
17. Phosphate Buffer Saline (**PBS**)
18. Thermoelectric Module (**TEM**)
19. 4-methylumbelliferyl β-D-cellobioside (**MUC**)
20. 4-methylumbelliferone (**MUF**)
21. Resistance Temperature Detectors (**RTD**)

Articles in Preparation for Publication

World-to-digital microfluidics interfaces for transformation and enzymatic assays

Ehsan Moazami, [1, 2] James Perry, [2, 3] Guy Soffer, [1, 2] Mathieu C. Husser,[2, 3] Steve C.C. Shih[1-3]*

[1]Department of Electrical and Computer Engineering, Concordia University, Montréal, Québec, Canada

[2]Centre for Applied Synthetic Biology, Concordia University, Montréal, Québec, Canada

[3]Department of Biology, Concordia University, Montréal, Québec, Canada

*Corresponding author

Tel: +1-(514) 848-2424 x7579

Email: steve.shih@concordia.ca

Chapter 1.   Introduction to Miniaturized Fluid Handling

In this section, we will introduce microfluidics in the bigger realm of miniaturization, describe the three dominant paradigms and briefly evaluate their potential for cell-based applications. From this review, we will draw a table comparing the three paradigms.

1.1   Historical Perspectives on the Miniaturization of Biology

Biologists first began shifting away from traditional glass tubes and dishes for bench-top biology in the 1950s when Dr. G. Takatsy described the first microtiter well-plates. [1] The invention of multi-well plates led to an unprecedented increase in throughput, having a number of wells with predefined volumetric capacities in the range of microliters to milliliters arranged in a standardized, rectangular matrix. Takatsy laid the foundations for early bench-top miniaturization and his contemporary counterparts still resort to such methods for high-throughput drug screening, enzymatic assays, cell-based assays, and countless other applications.

Towards the end of the twentieth century, high-throughput screening (HTS) became the gold standard for pharmaceutical drug discovery, where the limits of throughput and screening efficiency were stretched by creating new 384- and 1536-well formats. Such formats enabled higher experimental densities in parallel with lower experimental footprints due to reduced reagent consumptions along with higher statistical significance with facilitated experiment replication. HTS is now actively used in a wide-range of applications, from genomics to environmental sampling and from protein crystallization to cell-based assays.

HTS requires cutting-edge technologies at high precision to keep up with the number of samples being assayed in parallel, at a pace that is unachievable by manual labor. In the past few decades, automated liquid handling robotics (ALHR) have been developed to automate fluid handling and facilitate the handling of large numbers samples in microtiter plates. Despite the ground-breaking technological advances in such systems, robotics is often inaccessible given the high capital costs (can reach a few million USD), the excessive consumption of consumables (pipette tips, multi-well plates, etc.) and large volumes of reagents being consumed (media, drugs, cells, etc.). Attention is slowly shifting towards cheaper alternatives for biology miniaturization and automation, with higher content and quality of the data.

As progress was being made in miniaturizing benchtop experiments into microtiter plates, significant progress was being made in understanding fluid dynamics, notably Brownian motion and diffusion, by the combined efforts from Einstein[2] and Berg[3] in biological systems. In parallel, Taylor[4] had been examining liquid flow in micron-scale channels. The development of miniaturized chromatographic[5] and ink-jet technologies[6] enabled the innovation and implementation of "microfluidics" for biological investigation. Furthermore, the development of soft-lithography, solid etching and replica molding in PDMS, presented by the Whitesides group in 1998,[7] led to the popularization of microfluidic technologies. Microfluidic technologies are being extensively explored as an alternative to multi-well plates and led to the development of numerous technologies vulgarized as "labs-on-a-chip" (LOC) technologies.

LOC technologies are characterized by a miniaturization of experiments and integration of laboratory instruments onto tiny hand-held devices. With simple and cheap fabrication procedures, and handling of small volumes and samples, such devices bypass the need for expensive operating systems, and enable high-throughput and automation. Three paradigms have emerged and become

dominant in the midst of miniaturization. The first is microchannels, being the most popular paradigm, where bulk fluid flows through micron-sized dimension channels.[8, 9] The second is droplets-in-channel, where fluid is manipulated as discrete droplets in enclosed channels, where each droplet acts as an individual microreactor.[10, 11] Finally, digital microfluidics (DMF) is the manipulation of fluids as discrete droplets on an open array of electrodes.[12-14] I will briefly review all of these paradigms before venting the merits of DMF as a versatile liquid handling platform.

1.2   Microchannels

The most widespread form of microfluidics today is microchannels, also known as continuous channel microfluidics, where micron-sized dimension channels confine reagents. The liquid transport of such reagents is driven by pressure gradients from external (e.g. syringe pumps) or internal pressure sources. Fluid flow is enabled after injection of reagents into the chip either batch-wise or in continuous mode. In these systems, the flow is dependent on two conflicting forces: (1) inertia, the resistance of objects to changing their current state of motion and (2) viscosity, i.e. the resistance of a fluid to stress-induced deformations. The balance of these two forces is described by the dimensionless Reynold's number:

Equation 1.1: Reynold's number

$$Re = \frac{Net\ Inertial\ Forces}{Net\ Viscous\ Forces} = \frac{\rho v L}{\upsilon}$$

where ρ is the fluid density (kg/m^3), v is the mean velocity (m/s), L is the characteristic length of the system, and υ is the kinematic viscosity (m^2/s).

The dominance of one of these two forces over the other will determine whether the flow is turbulent (chaotic) or laminar (deterministic). When Re < 2000, the flow is laminar, when 2000

< Re < 4000, the flow is unstable and when Re > 4000, the flow is turbulent. Given the micron-size of these channels, the length can be estimated to around 10^{-6} m – this results in most microfluidic systems to be viscosity dominated, resulting in laminar flows with low Reynold's number regimes. Such laminar flow enables multiple streams of reagents to be constrained within a single channel without mixing.

Such a technology has been used in numerous biological applications, including chemical separations,[15] single cell/molecule analysis,[16] and simple reactions performing better at the microscale with high surface-to-volume ratio.[17] The surface area to volume ratio increases when the scale of volumes is reduced. This substantially increases heat and mass transfer rates, useful to speed up exothermic and endothermic reactions. The integration of microvalves relying on flexible membranes and pneumatic control layers on-device allows these devices to become compartmentalized high-throughput systems.[8, 18-20] Such compartmentalization enables multiplexing, by which ~ 10^6 independent compartments are formed, each containing volumes in the range of 10-100 picoliters.[18] Nevertheless, microvalves require complex fabrication techniques (1 compartment requires at least 1 valve) and precise alignment strategies to make a functional device. In addition, the number of inlets and external pressure sources such as syringe pumps increases the complexity in fabrication, costs, manual intervention and expertise. Such inherently complex fabrication techniques, coupled to the dependence on external equipment and complex tubing/device assembly often makes microchannels undesirable to implement in the daily workflows of biologists. In addition, the inability to efficiently mix reagents limits the breadth of potential applications.

1.3   Droplets-in-Channel

The droplets-in-channel paradigm is characterized by a two-phase flow, usually with water, oil and/or gas, in microchannels. Such a configuration enables the formation of pico and nano-liter droplets, that can be generated at rates in the thousands of droplets per second. These droplets can be merged, sorted and reacted on-demand.[10, 21, 22] Such devices are simple to fabricate and can operate at high-throughput (10-100 kHz) which makes them desirable for biological screening applications. Research and development in this field has been increasing control over individual droplets, for better in-channel guiding and sorting using rails,[23-25] laser forcing,[26] or electrostatic charging. [27-29]

The most significant advantages of such a miniaturized platform is the small size of working volumes, the high-throughput nature of reagent manipulation, the individuality of each droplet eliminating the risk of cross-contamination, different strategies to mix reagents within droplets and the ability to incubate and store these miniscule droplets for extended periods of time without evaporation. Bio-compatible surfactants are often used to stabilize emulsions, which allows live cells to be encapsulated, and fluorinated oils in the continuous phase allows sufficient gas exchanges to maintain cell viability for extended periods of time. Such advantages have garnered interest in numerous fields and applications, including magnetic-bead based assays,[30-32] single cell high-throughput studies,[33-35] protein crystallization[36] and chemical synthesis.[37]

Nevertheless, just like microchannels, droplet microfluidics requires pumps, complex tubing for inlets and outlets and other external equipment, which discourages certain researchers to move away from their traditional practices. Also, multi-step long-term applications are difficult to implement in such systems given that the speed of individual droplets makes the individual addressability of droplets complicated for reagent addition, staining and media exchange.

Furthermore, sorting and detection often requires optical systems and read-outs, and specialized microscopy analysis techniques, thereby complicating the process.

1.4 Digital Microfluidics

My research utilized a more recent technology developed in the realm of miniaturization called digital microfluidics (DMF), still in its infancy. Such a technology accurately represents the "lab-on-a-chip mindset", where all laboratory instruments and components are integrated onto a single hand-held device. The technology relies on the manipulation of picoliter-milliliter sized droplets on an array of electrodes. DMF is now being used in a wide-range of applications, with the advantages of reduced sample size, fast heat transfer and reduced reaction rates (explained by the high surface area to volume ratio) and is highly amenable to integration. A wide range of operations can be performed and reprogrammed on-demand, such as dispensing droplets from reservoirs, moving, merging, mixing and splitting into smaller droplets. One of the key advantages is that droplets can be addressed individually, where each reagent operated on a DMF device is isolated until merged with another reagent, and with each droplet acting as a discrete microvessel with no cross-talk with neighboring samples. Microchannels are very different in that respect where they operate with conventional flow and may be disturbed by hydrostatic and capillary flows. In addition, DMF devices are operated on generic platforms with simple configurations (M x N array), making them easy to operate and to reconfigure.

The individual addressability of samples makes DMF an inherently array-based technique. This makes DMF ideal for array-based biochemical applications. Despite certain challenges and disadvantages of DMF, we sought to harness the platform to automate gene editing, given that DMF allows a rational design approach to be used to target certain specific genes in an arrayed

manner, where experiments can be multiplexed and reprogrammed, cell-based assays can be performed on demand, and phenotypic readouts can be obtained, all in an automated manner.
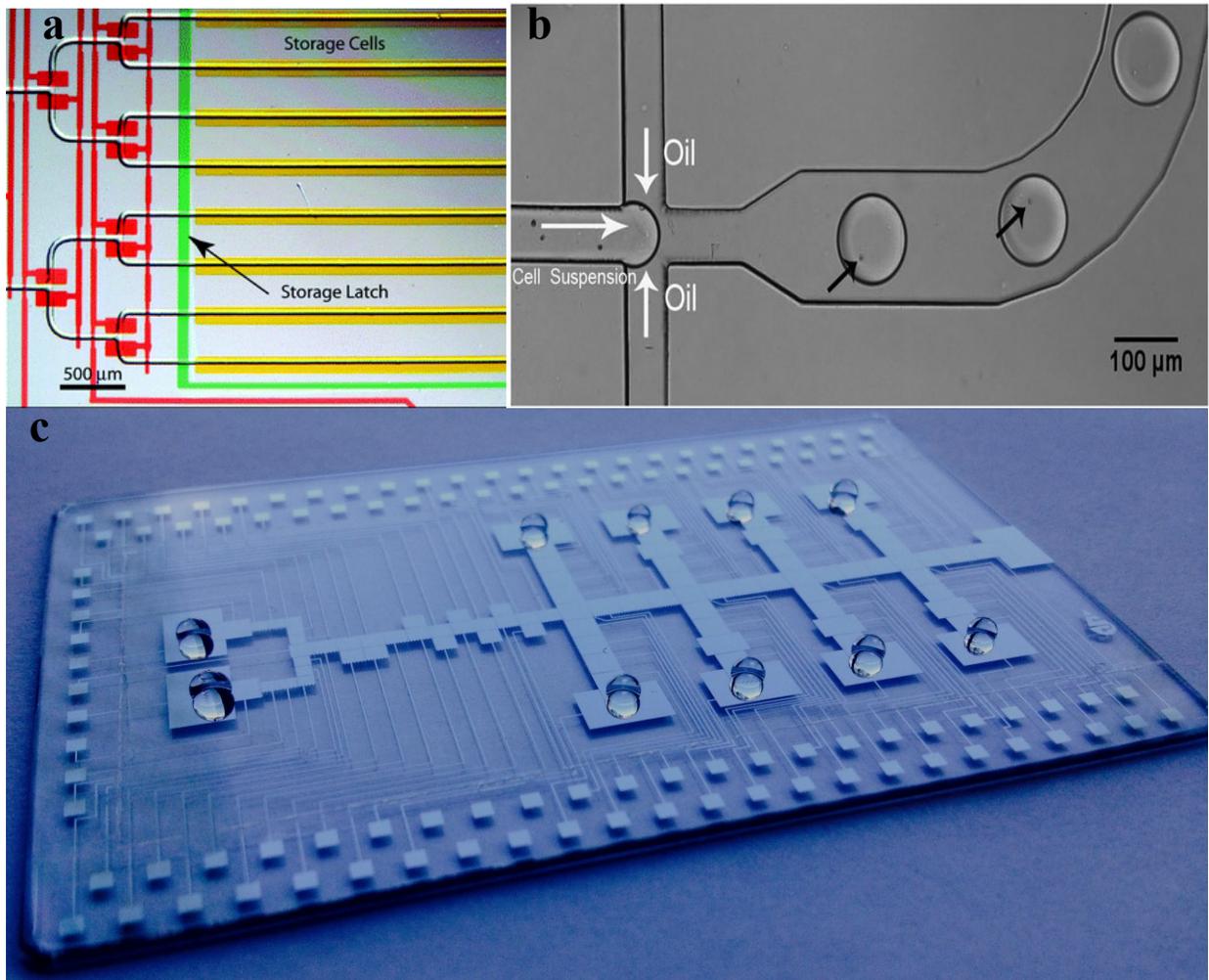
Figure 1.1 – Microfluidic Paradigms.

(a) Microchannels. Reproduced with permission from the Royal Society of Chemistry.[38] (b) Droplets-in-channel. Reproduced with permission from the Royal Society of Chemistry.[39] (c) Digital Microfluidics

1.5 Summary Table of Microfluidic Technologies

We hereby present a comparative table (Table 1.1) showing the state of microfluidic techniques versus traditional sampling in multiwell plates and show the advantages that each of these solutions offer in the market of miniaturization.

Table 1.1 – Comparative table assessing the state of miniaturization techniques.

Criteria	Well-Plate	Microchannel	Droplets-in-Channel	Digital Microfluidics
Cost of platform	$1-2 per plate	$5-10 PDMS device	$5-10 PDMS device	$6-10 per substrate
Reagent volume	μL-mL	nL-μL	pL-nL	100 pL-μL
Throughput	High	Moderate	High	Low
Automation	++	+	+	+++
Reprogramming	+	+	+	+++
External Parts	Robotics	Pumps & valves	Pumps & valves	None
Temperature Control	+	+	+	+++
Operations on device	None	Dispensing, separations, valving	Dispensing, mixing, splitting, merging, sorting	Dispensing, mixing, splitting, merging
No. of Scientists in the Field	> 100,000	> 1,000	< 1000	< 30

Chapter 2.   Special Focus on Digital Microfluidics

This chapter will provide an in-depth review of DMF theory, venting its merits as a versatile liquid handling platform, describe the fabrication methods, assess the potential for automation and finally comment on its amenability to cell culture.

2.1   Digital Microfluidic Theory

In the broad realm of biomimicry, scientists have been eager to control the surface wettability by fluids, in a similar way that nature has engineered "self-cleaning" lotus leaves or "fog-collecting" *Stenocara* beetle.[40] From this research drive emerged a phenomenon known as "electrowetting", by which a solid surface's wettability can be altered using electric potential.[41-43] Electrowetting-on-dielectric (EWOD) is a phenomenon that can be applied to control aqueous liquids by varying the electric energy across the micron-thick dielectric layer separating the liquid and the conducting substrate.[43] This phenomenon can be translated to a driving mechanism, where liquids can be shaped and driven along a path of electrodes. Fluid position can therefore be modulated by placing droplets on an array of electrodes coated with an insulator.[40] Electrical potential can be applied sequentially to adjacent electrodes on a path, and the droplets carrying various reagents can be moved on that array on-demand.

The reigning forces in EWOD can be separated into driving and resistive forces. The earliest theoretical attempts for estimating the driving forces were based on a thermodynamic approach using the Young-Lippman equation:

Equation 2.1: Young-Lippman equation

$$\cos\theta_w = \cos\theta_0 \frac{\varepsilon_0 \varepsilon_r V^2}{2\gamma t}$$

where θ_w and θ_0 are the wetted and static contact angles, respectively; ε_0 and ε_r are the permittivities of free space and of the dielectric, respectively; V is the applied voltage; γ is the liquid/filler media surface tension (air or oil); and t is the dielectric thickness. In this model, it is assumed that droplets are moved due to capillary pressure resulting from asymmetric contact angles across the droplet. In Equation 2.1, the contact angles are static and do not account for droplet motion after deformation. Therefore, the driving force F in this model can be expressed as:

Equation 2.2: Driving force using Young-Lippman

$$F = L\gamma_{LG}(\cos\theta_w - \cos\theta_0) = \frac{\varepsilon_0 \varepsilon_r L V^2}{2t}$$

where F is the driving force and L is the length of the contact line overlapping the actuated electrode. This driving force is often referred to as the "EWOD force".

The term "Digital Microfluidics" emerged upon the realization that the theory behind electrowetting does not apply to fluids with low surface tension, given that such liquids are readily moved on electrodes but do not exhibit a significant change in contact angle – this empirical result showed that large changes in contact angles are not a requirement for droplet movement. In addition, the thermodynamic approach fails to explain the liquid-dielectrophoretic force, which is predominant at high frequencies.

In fact, the wetting is an observable effect of the forces acting on the droplet. The most accurate way to estimate the forces on the droplet in DMF is to use a circuit diagram and adopting an electromechanical approach. The amount of energy stored in this system is calculated as a

function of the applied voltage frequency and droplet position along the direction of translation. Here is the Equation 2.3 representing the amount of energy, E, of the system:

Equation 2.3: Energy equation using electromechanical model

$$E(f,x) = \frac{L}{2}\left(x\sum_i \frac{\varepsilon_0 \varepsilon_{ri,liquid} V_{i,liquid}^2 (j2\pi f)}{d_i} + (L-x)\sum_i \frac{\varepsilon_0 \varepsilon_{ri,filler} V_{i,filler}^2 (j2\pi f)}{d_i} \right)$$

where L is the dimension of the droplet (estimated by the cross-section of the drop), $\varepsilon_{ri,liquid}$, $V_{i,liquid}$ and $\varepsilon_{ri,filler}$, $V_{i,filler}$ are the relative permittivity and voltage drop for the liquid and filler fluid portions of the electrode, respectively, and d_i is the thickness of layer i (corresponds to the dielectric, hydrophobic, liquid or filler layers). Differentiating the energy calculated in Equation 2.3 with respect to x yields the driving force as a function of frequency:

Equation 2.4: Force equation using electromechanical model

$$F(f) = \frac{\partial E(f,x)}{\partial x} = \frac{L}{2}\left(\sum_i \frac{\varepsilon_0 \varepsilon_{ri,liquid} V_{i,liquid}^2 (j2\pi f)}{d_i} - \sum_i \frac{\varepsilon_0 \varepsilon_{ri,filler} V_{i,filler}^2 (j2\pi f)}{d_i} \right)$$

The key advantage of the electromechanical model is that it takes into account the frequency of the applied voltage on droplets across each layer and portion of the device – it represents the stored energy that results in an applied force.

From this, we can calculate a critical frequency (f_c) for each device geometry and the liquids being operated.[44] Below the critical frequency, we can apply the equations relative to the EWOD model. The force that is driving the droplet at low frequencies comes from charges accumulation near the three-phase contact line, which are being pulled toward the actuated electrode electrostatically. The magnitude of this force depends on the capacitive energy stored within the dielectric. When we apply frequencies above f_c, an electric field gradient is generated

across the droplet, generating a liquid-dielectrophoretic force to pull the droplet toward the activated electrode. Here, the magnitude depends on the difference in permittivity between the liquid and filler medium (air, in our case). In DMF, droplets are manipulated by AC frequencies in the order of kHz and the majority of the voltage drops across the dielectric. When inserting this range of frequencies in Equation 2.4, we obtain an estimation of DMF forces with magnitudes in the range of µN, which can be applied to a wide range of fluids using driving voltages of 100-300V$_{RMS}$.

The driving electrostatic forces acting on the drop compete with counteracting forces. The first is the shear force between the droplet and the plates,[45, 46] which is highly dependent on local surface smoothness and heterogeneity, dictated by the quality of dielectric and hydrophobic coating and resulting nano- and micro- scale roughness of the hydrophobic surface. The second factor impeding droplet movement is the viscous drag force resulting from displacement of the filler fluid during droplet translation.[46] As soon as the driving force is greater than both the shear and viscous drag forces, droplet movement can be observed. Overcoming such movement limitations is critical in enhancing droplet movement, and the optimization lies in surface characterization, use of surfactants, device design and the device hydrophobicity.

We must note that for most DMF systems, the forces calculated by electrowetting and electromechanical models reach consensus. In this thesis, we are manipulating conductive liquids (media charged with salts) in air, which makes the energy stored in the filler portion of the electromechanical model negligible in comparison to that in the liquid portion ($\varepsilon_{ri,liquid} \gg \varepsilon_{ri,filler}$). In addition, the energy that is stored in the liquid layers are negligible in comparison to that stored in the dielectric layer ($d_{dielectric} = 7\mu m \; vs. \; d_{\frac{liquid}{filler}} = 140\mu m$).
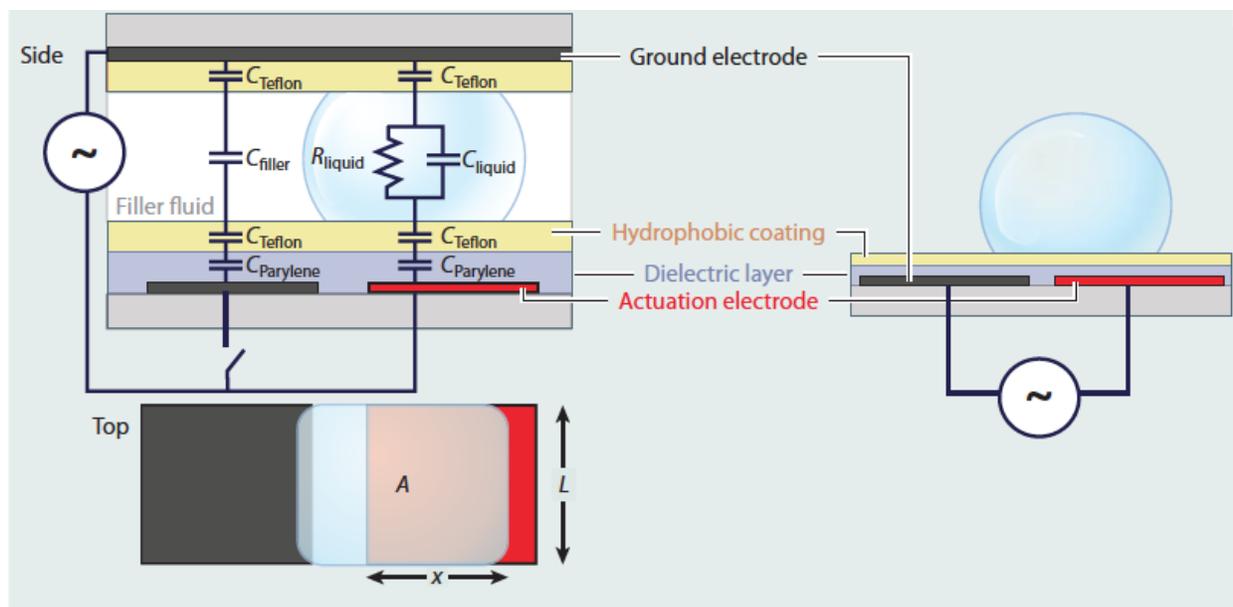
Figure 2.1 – Single-plate and two-plate configurations for DMF.

In the one-plate format, both grounding and high-voltage electrodes are on the same plane. In the two-plate format, the grounding electrodes is typically the same as the top-plate (i.e. covering plate) and the high-voltage electrode is on the bottom plate. Droplets are sandwiched between the two plates. (Image obtained from Choi et al.[47])

2.2 Digital Microfluidics and Automation

The greatest advantage of digital microfluidics is perhaps its amenability to integrating automation systems[48, 49] and coupling the platform to external detectors (or internal in-line detectors[50, 51]) for real-time or downstream biological analysis. [52, 53] The core of DMF automation systems interfaces with a DMF device which enables droplet movement with a standard set of basic instructions written by the user. The user will interact with the graphical user interface (GUI) to program a set of instructions to dispense, move and split droplets, merge droplets together and

13

to mix resulting samples and sort droplets for analysis (Figure 2.2). Such automation gives DMF the capacity to operate droplets in parallel on a single device, without the need for any valves or pumps.
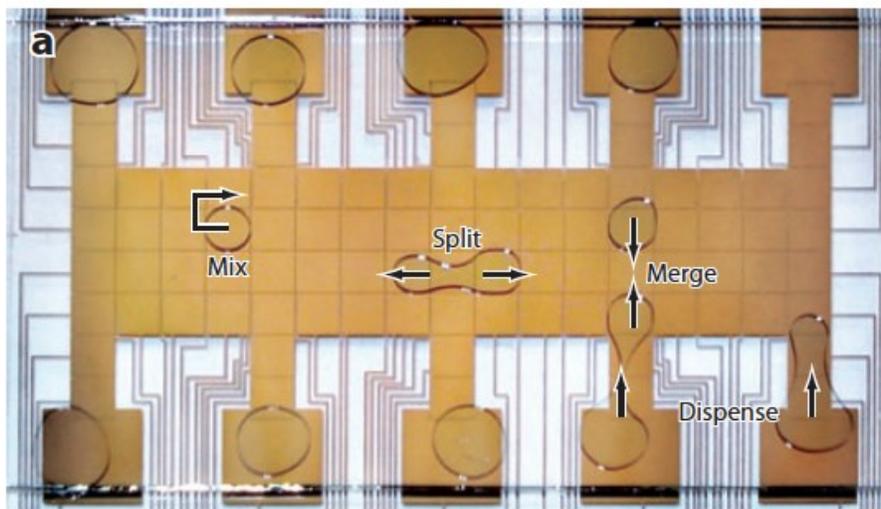
Figure 2.2 – Operations performed on a DMF device.

These operations include droplet dispensing, droplet splitting, droplet mixing, and droplet merging. (Image obtained from Choi et al.[47])

Typically, DMF automation systems rely on an array of relay switches, each of which is responsible for one individual electrode on the device and relays AC or DC voltages to it when instructed. The state of the switches is controlled through a computer and microcontroller. Specifically, our automation system (Figure 2.3) consists of a MATLAB program (Figure 2.4) that is used to control an Arduino Uno microcontroller. Driving input potentials of 130-270 V_{RMS} are generated by amplification of a sine wave output from a function generator operating at 10 kHz by an amplifier and delivered to the PCB control board. The Arduino controls the state of high-voltage relays that are soldered onto the PCB control board. The logic state of an individual solid-state

switch is controlled through an I^{2}C communication protocol by an I/O expander. This control board is mated to a pogo pin interface (104 pins), where each switch delivers a high-voltage potential (or ground) signal to a contact pad on the DMF device. See our GitHub registry (https://github.com/shihmicrolab/Automation) to assemble the hardware and to install the open-source software program to execute the automation system.

The ideal result of the DMF automation system is that every set of instructions would equate to a droplet movement (e.g., mix, dispense, split) towards the energized electrode. However, due to surface heterogeneity or roughness or the contents of the droplet, every application of a potential does not easily translate to a movement on the device. This behaviour is exacerbated when the droplet constituents contains cells or proteins as they tend to 'biofoul' the surface and render the device useless over a few actuations.[54, 55] Vo et al. describes published work from the Shih lab alleviates this issue through use of an image-based feedback system to monitor droplet movement in real-time and overcome droplet failure by providing additional driving voltages until the droplet completes the desired operation.[56]
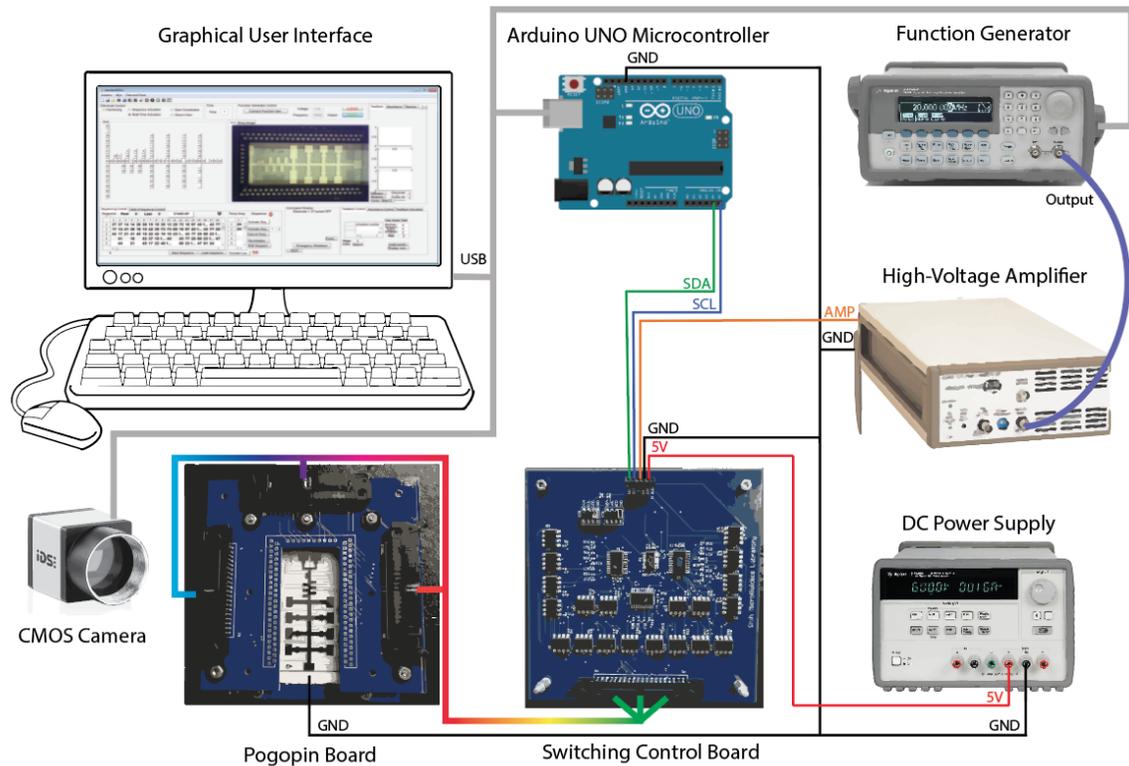
Figure 2.3 – Digital microfluidic automation system.

The device is connected via a pogopin interface in which electric potentials are applied to an electrode on the device. Potentials are controlled through a switching control board which are controlled by the graphical user interface and microcontroller. An external function generator and amplifier, and power supply is required to deliver the AC signals and to deliver 5V power to the system respectively.
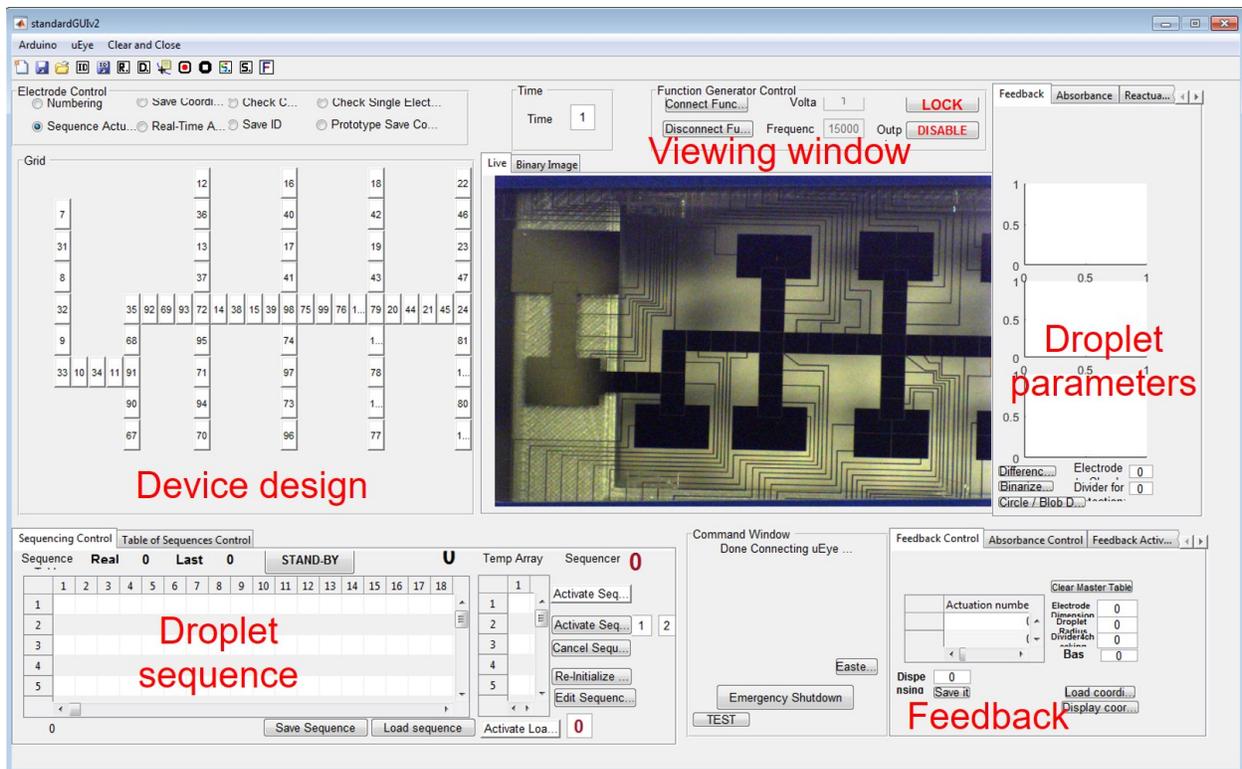
Figure 2.4 – Graphical User Interface for the DMF automation system.

The GUI consists of five different components: device design (to control the activation of an electrode), a live viewing window (to view droplet operations directly on the device), droplet parameters (high voltage and frequency), droplet sequences (automated droplet sequences), and feedback (to ensure droplet movement fidelity).

2.3   Current State of Digital Microfluidics

Digital microfluidics is equipped with many unique and useful liquid handling features and for this reason there is much enthusiasm in applying DMF to a myriad of applications such as chemical and enzymatic reactions, immunoassays, DNA-based applications, clinical diagnostics, proteomics, and cell-based applications.[47] Individual addressability (i.e. control) of droplets and

the amenability of integrating automation are two key advantages of the DMF technology in comparison with other types of microfluidic systems.

Despite the enthusiasm in using DMF, the technology still has not kept pace compared to other microfluidic technology (e.g., droplet microfluidics). There are still significant challenges that prevent its widespread adoption in industry-based or clinical-based laboratories. One such challenge is the integration of 'world-to-chip' interfaces that minimizes user intervention with the microfluidic chip. An ongoing 'world-to-chip' challenge has been the delivering of samples to the chip and the refilling of liquids to the microfluidic device. A second challenge is the integration of temperature control on the device since almost all (if not all) biological and chemical-based applications require cells, proteins, and DNA/RNA to be incubated at specific temperatures for these biological systems to function. Therefore, to increase adoption of digital microfluidics by the industrial and clinical communities there is a requirement of developing world-to-chip solutions to minimize user intervention.

Chapter 3. World-to-Chip Interface for Digital Microfluidics

This chapter is a review of the biological stakes that we will be addressing with our platform, presenting world-to-chip interfacing techniques with a special focus on reagent delivery system and temperature control on DMF chips, and comments on the technological limitations in operating world-to-chip interface today. This commentary will lead to the presentation of my thesis objectives.

3.1 Introduction to World-to-Chip and Current Techniques

There are several advantages in using a digital microfluidic platform: (1) the small working volumes (pL-µL volumes), (2) the high-throughput multiplexed nature of reagent manipulation, (3) the individual addressability of each droplet eliminating the risk of cross-contamination, and (4) the ability to automate different fluidic operations: dispense droplets from reservoirs, merge and mix droplets, and the ability to incubate and to store these miniscule droplets for extended periods of time without evaporation. A limitation for digital microfluidics is the integration of the device to the macroscopic world. [57] This limitation includes several aspects which includes delivering and refilling volumes on the microfluidic device, and integrating heating or cooling elements or external analytical-based detection systems. Below we review these aspects and discuss the current state-of-the-art for traditional and digital microfluidics.

3.2 Automated Reagent Delivery System Techniques

One of the stumbling roadblocks associated with successful miniaturization and automation of microfluidics is the requirement of delivering and refilling reagents to the chip.

Typically, there is a minimum practical volume (~ 1 µL) that can be introduced onto a microfluidic device, which limits the amount of volume that can be used on the chip unless it is refilled, or the initial volume is increased. One of the most common approaches to loading samples or storing large fluidic volumes has been the use of epoxy based adhesives integrated with traditional-microfluidic devices. [58] However, the use of adhesives directly on the device has known to cause leakage flow issues, contamination, and at times biochemical incompatibility. Another possibility is to use pumps and valves (see Liu et al. [59]), however, the pumps and valves concept is not suitable for digital microfluidics due to the complexity of fabricating these features on the device. There have been several digital microfluidic world-to-chip interfaces that have been useful for delivering reagents.
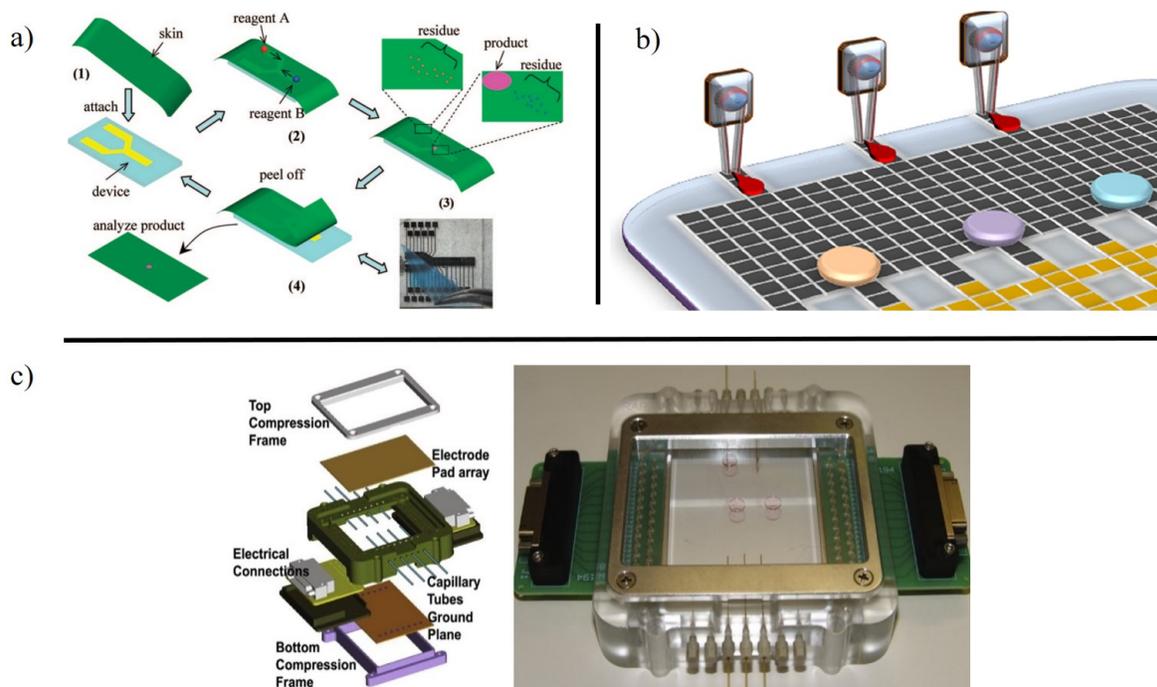
Figure 3.1 – Reagent delivery systems for DMF.

a) Schematic depicting the removable skin strategy in which a fresh piece of polymer is affixed to a DMF device and later can be peeled off repeatedly. Reproduced from [60]. b) A schematic showing

the integration of peristaltic pumps to deliver liquids to digital microfluidic devices. Reproduced from [61] . c) An image showing the integration of capillary tubes that are connected to an auto-sampler (not shown) for the delivery of liquids. A manifold was constructed to integration automation and the world-to-chip interface. Reproduced from [62] .

Yang et al.[60] (as shown in Figure 3.1a) developed a new strategy for digital microfluidics, relying on removable plastic coverings, or skins. This strategy facilitates virtually unlimited reuse of devices without concern for cross-contamination, as well as enabling rapid access to preloaded reagents. The key feature is that they were be able to avoid biofouling and consequently cross-contamination on the chip. However, the reconstitution of reagents is not a favourable method for cells and DNA.

Jebrail et. al.[61] (as shown in Figure 3.1b) developed a novel engineered system to deliver fluid through a peripheral macroscale module through the space between the two DMF plates. They used this system for chemical processing of RNA in blood. They collected target analytes from a macroscale sample and efficiently transferring them to a DMF device for further manipulation in microscale volumes. A key result is that they were able to manipulate a real blood sample on the chip with volumes of 380 µL and that on-chip reactions were faster by two times and reagent consumption was reduced by 12 times compared to traditional methods. However, the use of a peristaltic pump to deliver the reagents to the device can be a challenge to setup if the number of reagents increases.

Kim et. al. [62] (as shown in Figure 3.1c) developed a DNA processing system consisting of a central DMF hub interfaced through novel capillary interconnects to a number of external processing modules. Their preliminary efforts have demonstrated the flexibility and reproducibility with which fluids may be transferred to and from the DMF device through the in-

plane capillary interface. Although, the system allowing both continuous-flow and droplet-based sample manipulations to be performed in one integrated system, however, use of pumps and valves to deliver the reagents to the device is a limiting factor in their approach.

There are currently different techniques for fabricating microfluidic devices, such as micro-machining, soft lithography, embossing, *in-situ* construction using injection moulding and laser ablation, which are used for large-scale replication and production. Some of these techniques require much space to hold multiple pieces of equipment, are labour intensive (multiple step processes to make final product), cause time wastage when making a change in design, and suffer from limited availability of biological materials. For small-scale production such as analysis in a laboratory environment, soft lithography, a multiple step process, is the current gold standard. A quick and easy fabrication of microfluidic devices will be preferred as cell biologists may not necessarily have the time to learn the fabrication process. Recently, advancements in 3D printing in terms of resolution and speed have helped to simplify the fabrication process of microfluidic devices into a single step. 3D printing technology is an alternative for connecting the world-to-chip for delivering fluids. 3D printing has become an attractive tool to fabricate measurement setup components. [63-67] It has several advantages as it allows the rapid printing of complex geometric structures without the complexity of etching or dissolution fabrication techniques. Furthermore, modulation has been an inherent part of 3D printing and it has become a desired choice for world-to-chip interfaces with microfluidics. [63, 68-70]
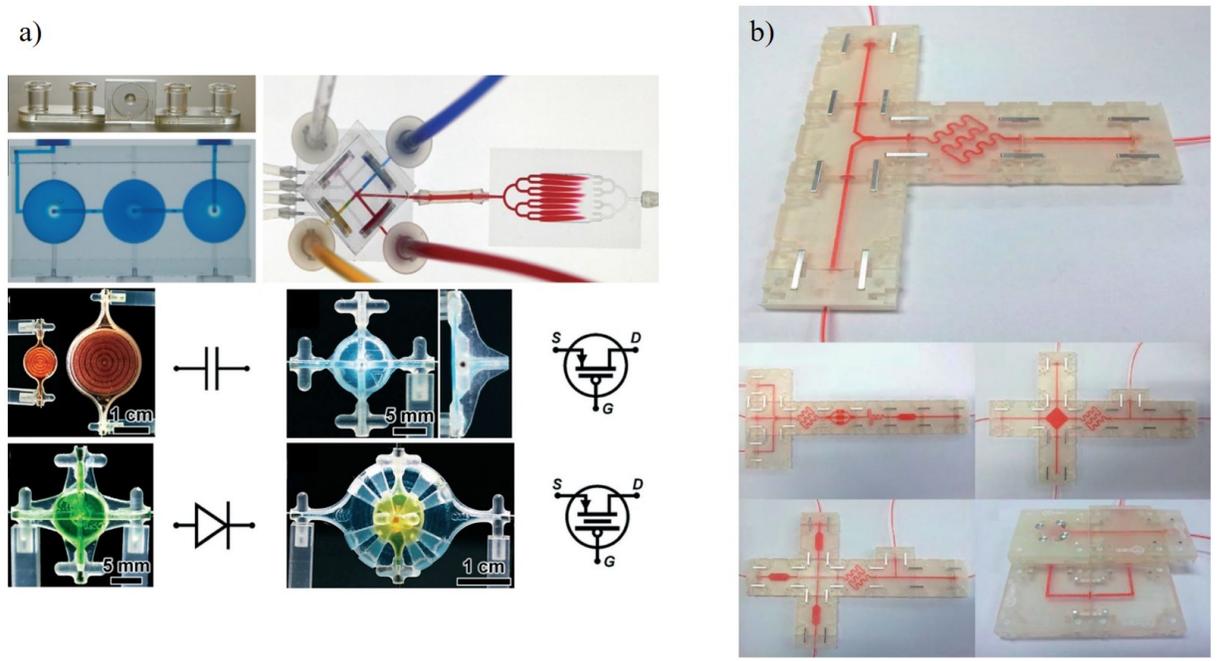
Figure 3.2 – 3D printed microfluidic devices.

a) 3D-printed valves and pumps at low cost with transparent biocompatible plastics to automate fluid handling and manipulation. Reproduced from [66]. b) This is a module-based 3D-printed microfluidics system. Different application could be customized by connecting modules. The Figure shows several possible applications. Reproduced from [70].

For example, Bhattacharjee et. al. from Folch lab [66] (as shown in Figure 3.2a) have designed SL-printed diaphragm valves and peristaltic pumps designed for microfluidic automation. The valve is operated pneumatically. They 3D-printed valves and pumps at low cost with transparent biocompatible plastics to automate fluid handling and manipulation in the biotech and biomedical industry, replacing costly human labor and even robotic dispensers. However, to design a truly large scale integrated microfluidic circuit, further miniaturization of the dynamic microfluidic elements is crucial. Improvements in the 3D printing process such as better resolution and higher-biocompatibility resins will be required.

Lee et. al. [70] (as shown in Figure 3.2b) developed a rapid, user friendly and cost-effective fabrication of module-based microfluidic components using a 3D printer. The designs were directly printed into functional 3D modules. Different scenarios for module assembly displayed their functionality and recyclability. The varied modules designs were firmly connected using metal pins and rubber O-rings. The inserted O-rings perfectly sealed the interconnections between the modules more firmly and prevented any solution leakage. The simple and easy module assembly and reconstruction are suitable for expansion of microfluidics to non-expert users.

Although the aforementioned approaches are very promising in the field of microfluidics, all of them have only been applied to the traditional microfluidics. The integration of 3D printing with digital microfluidics would be an inexpensive approach for delivering reagents to the system. We believe this would improve the performance of reagent delivery on digital microfluidic devices.

3.3   Integrated On-chip Temperature Control

A second world-to-chip interface that is commonly integrated with microfluidic devices is temperature control on a chip. Temperature control is essentially required for most biological experiments which requires execution under a controlled temperature (either heating or cooling temperatures). In macroscale experiments, temperature control is performed by placing the sample tubes inside a temperature-controlled incubator for a specified time. In microscale experiments, temperature control (either in the form of constant or gradient) has been one of the major challenges to incorporate on a chip. The commonly used techniques for heating/cooling on chip has been the integration of external temperature elements (i.e. Peltier modules or heating elements) directly on the chip,[71] or the fabrication of channels or electrodes for supplying heating and

cooling temperatures,[72] Both are capable of generating accurate temperature profiles, however, many of them have not integrated the control and may limit some potential biological and chemical-based applications. Although there has been a vast number of papers related to incorporating heating/cooling on microfluidic device,[72] I review several digital microfluidic papers that integrate temperature control.
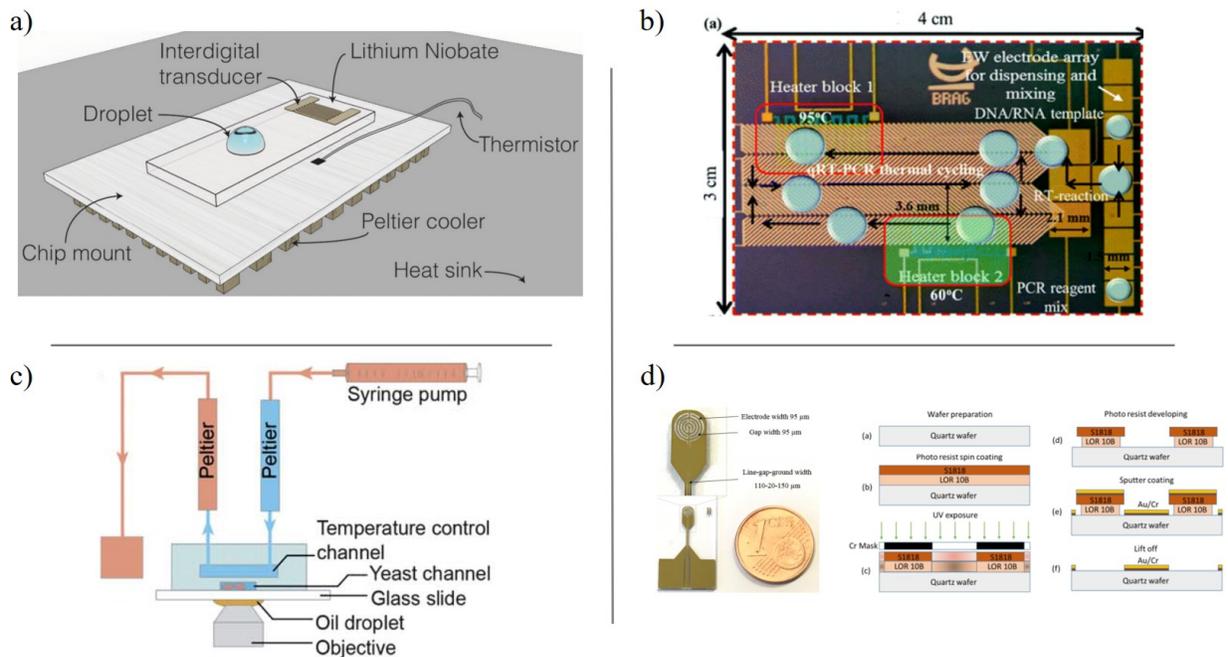
Figure 3.3 – Digital microfluidic devices with integrated heating.

a) Experimental schematics, with a thermal camera mounted from above (not shown). The setup consists of four parts: the gold-patterned LN SAW chip with hydrophilic wells; an aluminum chip mount (with thermistor temperature sensor for Peltier controller feedback); a Peltier cooler; and a large heat sink. Reproduced from [72]. b) A microfluidic device which consists of three layers: a chromium micro-heater and a resistance temperature detectors (RTDs), a gold/chrome layer, and Aluminum layer. Reproduced from [73]. c) A fluidic controlled Peltier system that is integrated

externally from the device. Reproduced from [74]. d) A gold/quartz fabricated micro-heater to be used in digital microfluidic devices to provide uniform heat for small droplets. Reproduced from [75].

Shilton et. al. [72] (as shown in Figure 3.3a) studied SAW (Surface Acoustic Waves) driven direct microfluidic droplet heating over the range of frequency (50−900 MHz) and power (up to 25 dBm) typically used in SAW-microfluidic processes in lab-on-a-chip devices. Acoustic heating-driven temperature changes reach a highly stable steady-state value in ~ 3 s, which is an order of magnitude faster than previously published. This method can be exploited for fast and highly stable control of chemical and biological reactions, and performed with complementary SAW-driven processes such as on-chip mixing, droplet translation, and particle separation for integrated devices.

Prakash et. al. [73] (as shown in Figure 3.3b) designed a microchip utilizing electrostatic/droplet-DEP (D-DEP) electro-actuation method and integrated thermostatic zones (micro-heaters and resistive temperature sensors) to achieve single qRT-PCR amplification of *in vitro* synthesized influenza viral RNA. The micro-device consists of: (1) an array of photo lithographically patterned chromium micro-heaters and resistance temperature detectors (RTDs), (2) a photo lithographically patterned gold/chrome overlay for electrical connections to the micro-heaters/RTD sensors, (3) a second photo lithographically patterned aluminum layer for D-DEP electrodes and (4) Au/Cr metallization for the EW track. These three metal layers were electrically isolated and passivated using a dielectric stack of silicon nitride (Si_3N_4 thickness: 500 nm), to prevent sample electrolysis during electro-actuations. Although the fabrication of resistive heaters

on the device can avoid external integration challenges, the multiple layers of photolithography fabrication and metal deposition can be expensive.

Casquillas et. al.[74] (as shown in Figure 3.3c) developed a disposable microfluidic device that enables fast temperature changes practical for biological experiments involving temperature-sensitive mutants and high spatiotemporal resolution imaging. The device is easy to fabricate and use in conventional cell biology laboratories and requires no modification to the current microscope setup. In addition, our device with two separate layers allows the cell layer to be adaptive, easily modifying cell shape or medium chemistry with new cell channel designs. Although this method is very efficient, but the lack of closed-loop temperature control to adjust and optimize temperature gradient on the device limits temperature-sensitive experiments.

Markovic et.al.[75] (as shown in Figure 3.3d) reported on a 4 GHz microwave droplet heater for digital microfluidics. The uniplanar device was fabricated using a gold-on-quartz process and was optimized for uniform heating within a 1 µL droplet. However, these approaches (and with Shilton et al.), both require either complex fabrication process like metal deposition or it requires external pumps for reagent delivery which poses challenges in scaling-up an assay that includes multiple reagents or conditions.

3.4 Thesis Objectives

The main objective of my thesis is to develop and to integrate world-to-chip interfaces on a digital microfluidic device. Specifically, I focused on designing two main world-to-chip interfaces, namely, (1) an automated reagent delivery system that will allow the refilling of fluids in the reservoir, and (2) the integration of closed-loop temperature control. To show the utility

and functionality of my system, I have validated these world-to-chip interfaces by applying them to two common biological applications: (1) bacterial transformation and (2) enzymatic assays. My research was segmented into three aims:

- **Aim #1:** To develop a reagent delivery system in an automated format to deliver the reagents to the reservoirs on-chip using 400 µL in volume.

- **Aim #2:** To integrate two thermoelectric Peltier elements to the DMF chip to have heating and cooling process on-chip simultaneously and validate the results by simulation.

- **Aim #3:** To apply aforementioned features to multiple biological process including bacteria transformation and enzymatic assay as a proof of principle.

Chapter 4.   Materials and Methods

This chapter provides a complete description of my methods, both on the biology and engineering side, to develop a functional world-to-chip interface for digital microfluidics. Also explains on how we integrate two different systems to digital microfluidics including 1) reagent delivery system and 2) temperature control system to build our platform.

4.1   Reagents and Materials

All general-use reagents were purchased from Sigma, unless specified otherwise. *E.coli* DH5α and BL21 and pFAB4876 and pSB1C3 vectors (see Appendix Information Table A1; Fig. 5.8 for plasmid maps) were generously donated from Dr. Vincent Martin. Mini-prep kits (cat no. BS413) were purchased from BioBasic (Amherst, NY). Pluronics F68 (Block Copolymer Surfactant) was also purchased from Sigma. $CaCl_2$ was purchased from Thermo Fisher Scientific.

Microfluidics device fabrication reagents and supplies included chromium coated with S1811 photoresist on glass slides from Telic (Valencia, CA), indium tin oxide (ITO)- coated glass slides, RS = 15-25Ω (cat no. CG-61IN-S207, Delta Technologies, Loveland CO), FluoroPel PFC1601V from Cytonix LLC (Beltsville, MD), MF-321 positive photoresist developer from Rohm and Haas (Marlborough, MA), CR-4 chromium etchant from OM Group (Cleveland, OH), and AZ-300T photoresist stripper from AZ Electronic Materials (Somerville, NJ). TEM/Peltier module from TE technology (MI, USA). For 3D printing, polylactic acid (PLA) material were purchased from 3Dshop (Mississauga, ON, Canada). 3-(Trimethoxysilyl) propyl methacrylate solution for silanization from Sigma (cat no. 440159). Parylene C pellets were purchased from Speciality Coating Systems (Indianapolis, IN).

4.2   Microfluidic Device Fabrication and Operation

Devices were designed using AutoCAD 2017 (Autodesk, San Rafael, CA) and fabricated in the Concordia cleanroom. The DMF fabrication procedure followed a previous protocol[56, 76] using high resolution 25,400 dpi transparency masks printed by CAD/Art services. Briefly, glass substrates pre-coated with S1811 photoresist (Telic, Valencia, CA) were exposed to UV for 8 s on a Quintel Q-4000 mask aligner (Neutronix Quintel, Morgan Hill, CA) to imprint the transparency masks design. These were developed in MF-321 for 2 min with shaking and rinsing with DI water. Developed slides were then baked at 115 °C for 1 min before etching in CR-4 chromium etchant until the pattern was clearly visible. The remaining photoresist was then removed in AZ-300T stripper for 2 min. After rinsing with DI water and drying, a silane solution comprising de-ionized water, 2-propanol and (trimethoxysilyl)-propyl methacrylate (50:50:1 v/v) was added to the devices in a Pyrex dish for 15 min. Devices were primed for dielectric coating with 15 g of Parylene-C (~7.2 μm thickness) in a SCS Labcoater 2 PDS 2010 (Specialty Coating Systems, Indianapolis, IN), and coated with Fluoropel PFC1601V (Cytonix, Beltsville, MD) in a Laurell spin coater (North Wales, PA) set to 1500 rpm for 30 s with 500 rpm/s acceleration followed by 10 min baking at 180 °C.
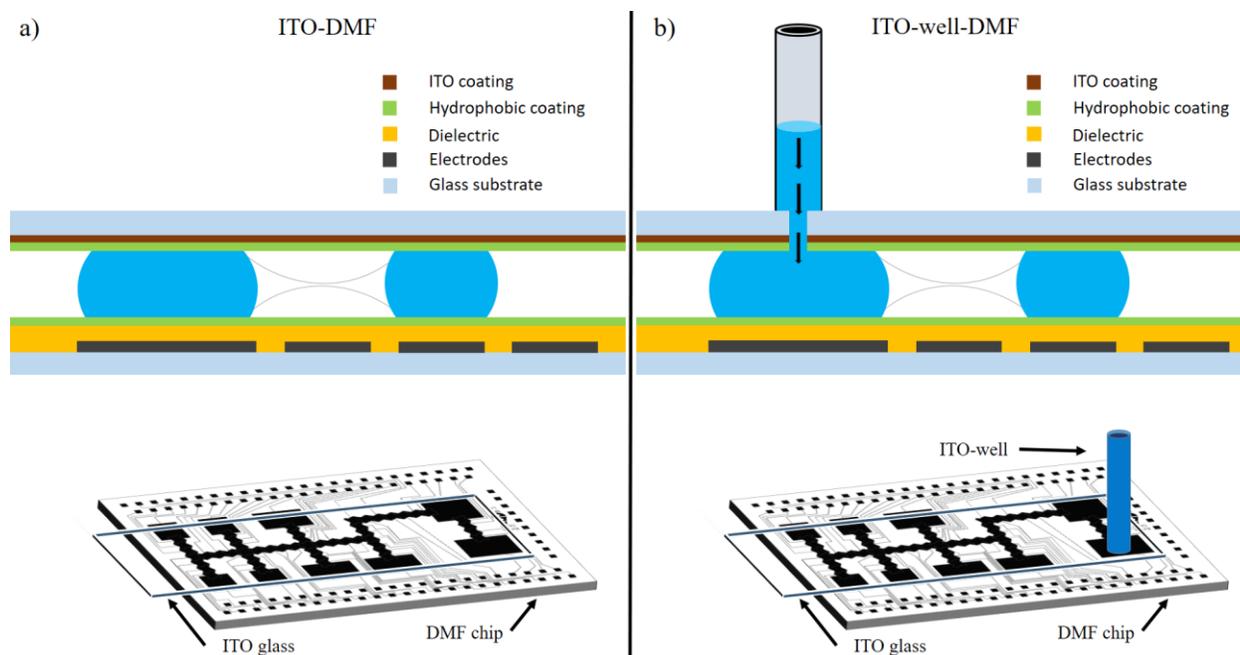
Figure 4.1 – Reagent delivery interface for digital microfluidic devices.

a) ITO-DMF is the typical two-plate setup used for digital microfluidics to automate liquid handling on device. b) ITO-well-DMF is the new world-to-chip system for reagent delivery on device. It consists of a 3D printed well integrated on top of the ITO top-plate which is aligned to an electrode (i.e. reservoir) on the device. Approximately 400 μL of liquid can be stored in the 3D printed well.

Prior to experiments, two types of top-plates were prepared – ITO-DMF or ITO-well-DMF (Figure 4.1). ITO-DMF were coated with FluoroPel PFC 1601V by spin coating and then post-baked as described above. For ITO-well-DMF, 1 mm diameter holes were drilled with using a Micromill (Proxxon MF 70, S.A. Wecker, Luxemburg) with a diamond drill bit (dia. 1.00 mm, L = 38 mm, diamond tip length: 3.50 mm, shank: 0.70 mm; ordered from KLY Amazon) on ITO-

DMF slides. These were diced into 25 mm x 75 mm pieces and were coated with Fluoropel PFC1601V and post-baked using the conditions described above on both sides. A 3D-printed well (with 1 mm diameter holes; see Figure 4.1b) is coated with Fluoropel (using a cotton swab) and were aligned directly on top of the holes on the ITO and glued (LePage super glue, Mississauga, Ontario) to the glass and dried for 5 min at room temperature. Both of these ITOs were joined to the bottom substrate with two pieces of double sided tape, resulting in an inter-plate gap of ~140 µm.

A custom-designed fabricated device was used in this study for bacterial transformation and enzymatic assays. After combining the top and bottom plates, the DMF device was primed to be interfaced through our automation system (see our online GitHub repository: [https://github.com/shihmicrolab/Automation]) that will automate the droplet movement on the devices. Electrodes were typically switched using solid-state relays which were controlled using an in-house program that applied 160 V_{RMS} at 15 kHz to the electrodes in a pre-programmed sequence.

4.3 Designing, Fabrication, and Operation of the Reagent Delivery System

3D printed wells were designed using Fusion 360 3D CAD/CAM design software (Autodesk, CA United States). The design was printed using on-demand printing using the Ultimaker 2+ extended (Shop3D, Mississauga, ON, Canada). All cylindrical wells were printed on polylactic acid (PLA) with an outer diameter of 8 mm and with a height of 45 mm and a 1 mm diameter hole (Figure 4.2).
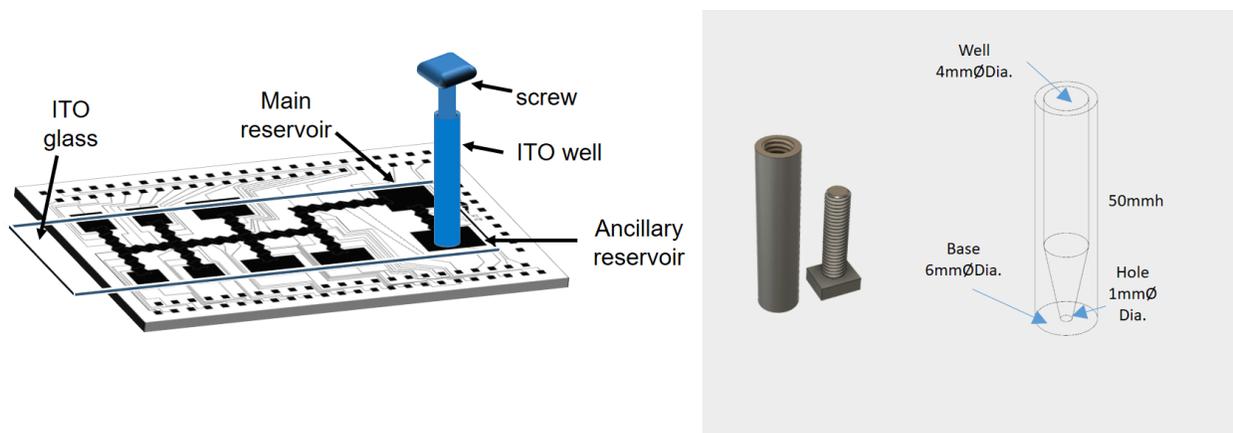
Figure 4.2 – Design and configuration of the 3D printed well.

a) The configuration of the 3D printed well on the DMF device. A plunger is added to the well to pressurize the liquid inside the well and to deliver the liquid into the reservoir. b) The design of the 3D printed well. Inside is a conical design with the dimensions as shown.

For 3D printing, STL files were generated and converted to gcode format using Acura 3D conversion with the following settings: nozzle - 0.4 mm, material – PLA, and profile - high quality. In the print setup settings, the recommended button was checked, the infill parameter was checked as 'Dense' and the helper parameter checked as 'Print Build Plate Adhesion and Print Support Structure'.

To use the well as a reagent delivery system, typically ~ 400 µL of fluid is pipetted into the threaded well and a screw was fabricated to control the delivery of the fluids into the reservoir. The device used two reservoirs for reagent delivery – a main reservoir for active dispensing of a unit droplet and an ancillary reservoir for refilling the main reservoir (Figure 4.2). The well (which was placed on the ITO top-plate) was aligned at the center of the ancillary reservoir. The operations

to refill reservoirs would proceed in the following three steps (Appendix Figure A.1): (1) the threaded plunger delivers liquid from the well to the ancillary reservoir on the chip, (2) a liquid neck is created from the ancillary to the main reservoir and the volume in the main reservoir is measured via impedance (Figure 4.3), and (3) when the volume reached a target of 7 µL in the main reservoir, the liquid neck is split by actuating the ancillary and main reservoir. This process is repeated for every unit droplet dispensed from the main reservoir. The impedance circuit to measure delivered volumes from the well is attached to the device top-plate (i.e. ITO top plate) and consists of a 10 kΩ resistor in series with the digital microfluidic device. A potential of 80 V_{RMS} was applied to the ancillary reservoir and the output of the circuit, V_{read}, is measured across the resistor as shown in Figure 4.3. The voltage is correlated with the fluid volume which was delivered directly on the device. This process of measuring the volume using the impedance circuit is repeated for every refilling step.
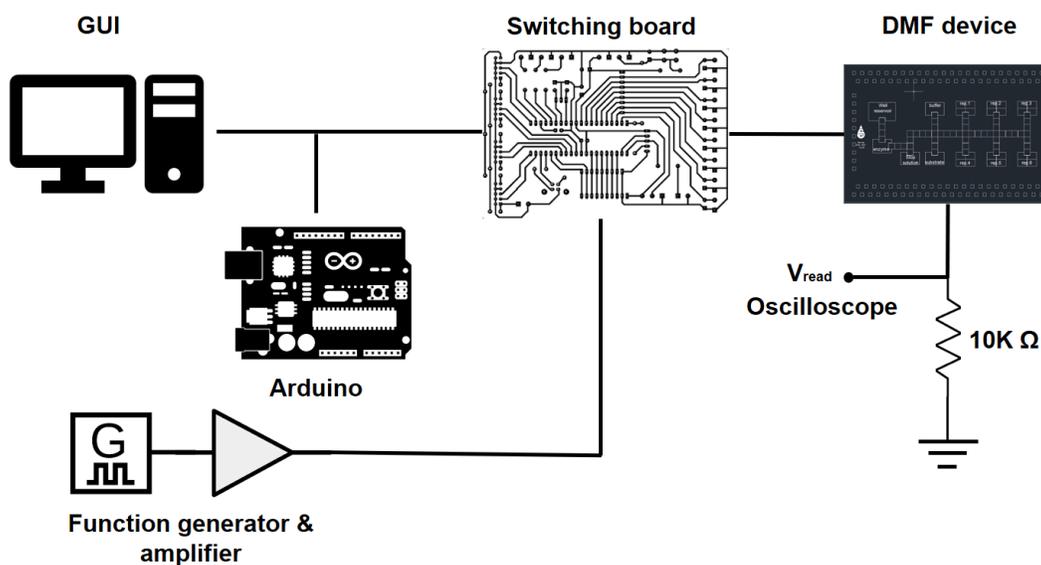

Figure 4.3 – Impedance measurement circuit to measure fluid delivery on the device.

The circuit consists of a resistor and the potential (V_{read}) is measured to correlate the amount of

The circuit consists of a resistor and the potential (V_{read}) is measured to correlate the amount of fluid to the potential.

4.4   Peltier Design, Operation, and Simulation

A 20 x 40 mm Peltier (TE technology INC, Texas, USA) was integrated below the DMF device that will be used to provide cooling (4 °C) and heating (42 °C) temperatures for procedures related to on-chip transformation. The Peltier was integrated with a 3D printed module with four 3D printed screws that can be interfaced with the DMF device. A 20 x 40 x 5 mm aluminum heating block was placed on top of the Peltier with a 1.5 mm drilled hole at the center of the block (Figure 4.4). The control hardware circuit for changing the temperature consisted of an Arduino microcontroller (Arduino Uno, Italy), a driver motor (consisting of two half-bridge driver chip and low resistance N-channel MOSFET) (Amazon, Mississauga, ON, Canada), and a resistance temperature detector (Building Automation Products, Inc., Gays Mills, WS, USA) placed inside the hole of the aluminum block. The hole was filled and sealed with thermo-paste (GC electronics, Rockford, IL) to secure it in place. Finally, the bottom of the aluminum heat block consisted of a 12 V_{dc} cooling fan which was responsible to dissipate the excess heat produced by Peltier for rapid temperature changes.
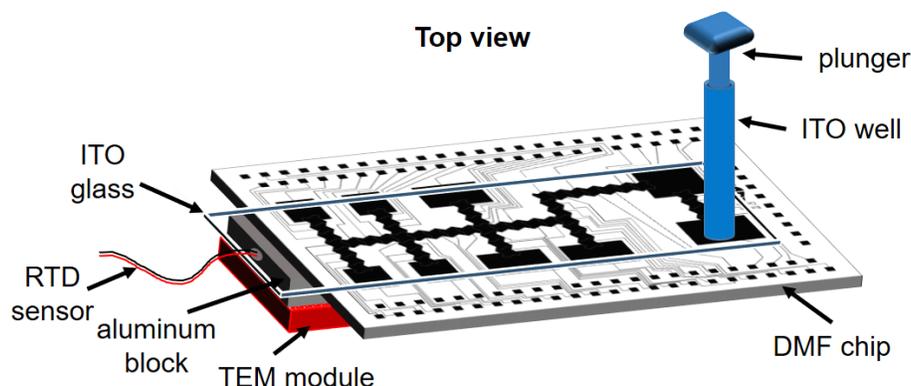

Figure 4.4 – Thermoelectric module (TEM) integrated to the DMF chip.

The TEM is attached to the aluminum block to improve the heat transfer properties of the module. An RTD (resistance temperature detectors RTD) sensor is placed inside the Al block to measure the temperature for closed-loop control.

For open-loop control, the Peltier was connected to a DC power supply through a MOSFET dual H-bridge driver. The driving current was controlled by an Arduino Uno microcontroller which was programmed by the user. Generally, the Peltier was set to operate in 4 ºC for 60 s, then was rapidly increased to 42 ºC for 60 s followed by a decrease to 4 ºC again for 120 s.

For closed-loop control, a proportional-integral-derivative (PID) based software code was written in MATLAB (MathWorks, MA USA) and integrated with Peltier system (as the open-loop control). Simulations of the temperature control were executed by changing rise time, over shoot, settling time, and steady-state error values as shown in Equation 4.1.

Equation 4.1: PID closed loop control system.

$$u(t) = K_p \mathrm{e}(t) + K_i \int_0^t \mathrm{e}(t')\, \mathrm{d}t' + K_d \frac{\mathrm{d}_e(t)}{\mathrm{d}t}$$

where, K_p, K_i and K_d represent gain coefficients for the proportional, integral, and derivative terms respectively, e(t) represent the error between the setpoint value and the process variable, and u(t) was a controller output. The chosen values for K_p, K_i and K_d are 15, 1.2, and 0.5 respectively.

To simulate the closed-loop system, we modeled the PID controller using the equation shown above and the TEM was modeled as a thermodynamic system (similar to ref [77]). The TEM model consists of thermopiles that are connected electrically in series to increase the operating voltage and thermally in parallel to decrease the thermal resistance and is sandwiched between two

ceramic plates for uniform thermal expansion. There are four main energy processes taking place in the TEM (Figure 4.5):

- Thermal conductivity

- Joule heating

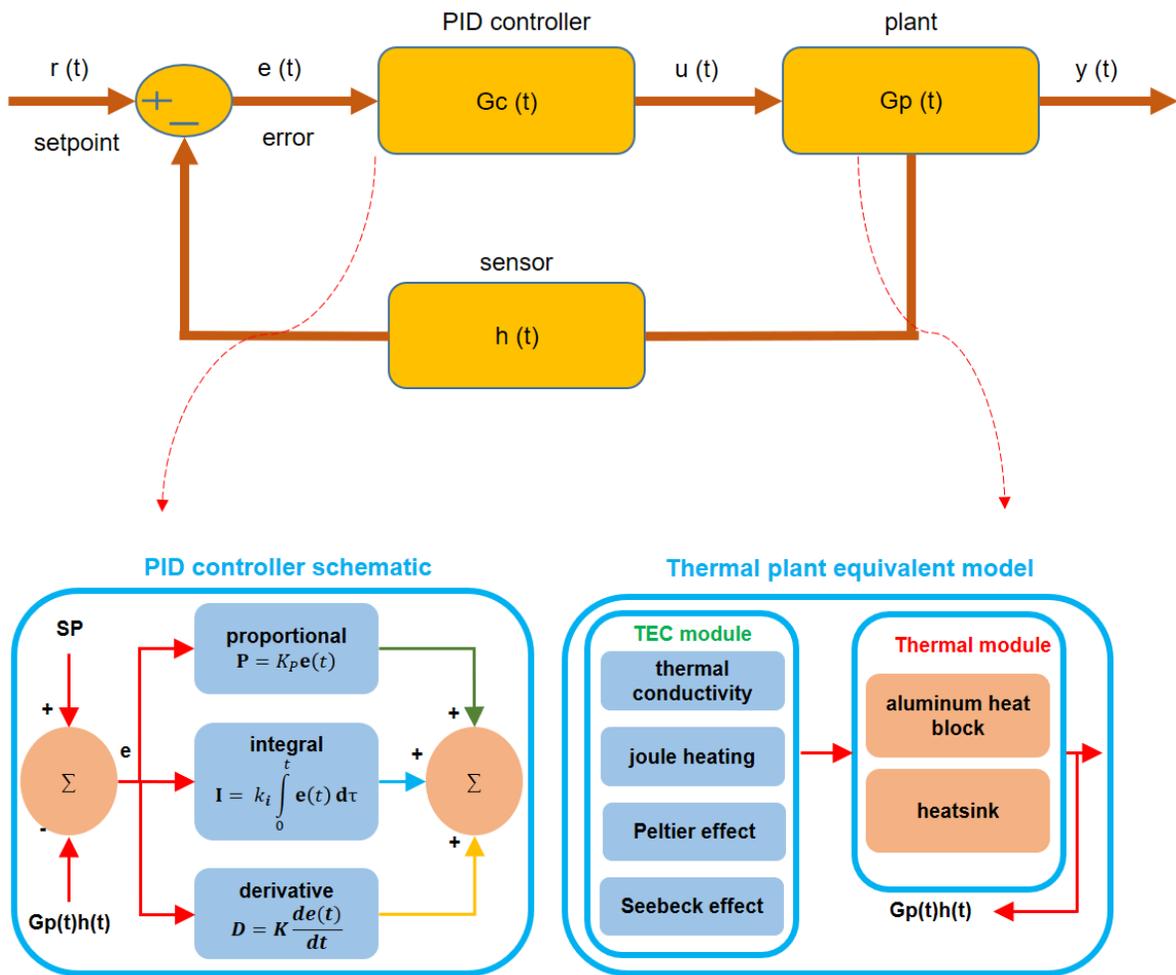- The Peltier cooling/heating effect and

- The Seebeck effect

Figure 4.5 – Thermoelectric module (TEM) thermodynamic plant modeling.

The modeling consists of two modules: thermoelectric and thermal. The TEM module consists of four components: conductivity, joule heating, Peltier effect, and Seeback effect. The thermal module consists of two modules: the Al heat block and the heatsink. All components are modeled by equations.

Table 4.1 showed all the parameters and equations were used to simulate a Peltier. A more detailed description of the energy processes and Simulink models used, are shown in the Appendix, thermal plant section.

Table 4.1 – Equations and parameters used to model the closed-loop thermoelectric module

Process	Equation	Parameter
Thermal conduction	$Q_{th} = -\Delta T * K_{th}$	K_{th}: Thermal conductivity coefficient of TEM = 0.39
Joule heating	$Q_j = I^2 R$	R: TEM internal resistance = 1.4Ω I: drawn current
Peltier cooling/heating	$Q_{pa} = S_m * I * T_h$ $Q_{pe} = S_m * I * T_c$	S_m: Seebeck coefficient = 0.018, I: drawn current, T_h: hot side temperature (K), T_c: cold side temperature (K)
Seebeck	$V_s = S_m * \Delta T(T_h - T_c)$	S_m: Seebeck coefficient= 0.018, T_h: hot side temperature (K), T_c: cold side temperature (K)
Heat transfer equation in TEM	$Q_{ta} = Q_{pa} - 0.5Q_j - Q_{th}$ $Q_{te} = Q_{pe} + 0.5Q_j - Q_{th}$	Q_{pa}: Peltier heating, Q_{ta}: Peltier cooling, Q_{th}: Thermal conduction,
Aluminum heat block temperature	$T_h = \dfrac{\int((T_{amb} * K_{th}) + Q_{te})}{Alum.\ thermal\ mass}$	Q_{te}: total heat transfer (hot side), K_{th}: thermal conductivity of Aluminum = 0.03, T_{amb}: room temperature in °C, Aluminum *thermal mass = 12.776*

Heat sink block temperature	$$T_c = \frac{\int((T_{amb} * K_{th}) + Q_{ta})}{Heatsink\ thermal\ mass}$$	Q_{ta}: total heat transfer (cold side), K_{th}: thermal conductivity of metal = 10, *Heatsink thermal mass = 200*

4.5   Competent Cell Preparation for Bacterial Transformation

On day 1, a single bacterial colony (2 to 3 mm in dia.) (from the streaked plate using the -80 °C stock) was inoculated in 5 mL of LB in a 20 mL flask overnight (about 12 to 14 h) at 37 ºC, 220 rpm. On day 2, 6 mL of the culture was added into 600 mL of fresh LB medium and incubated in 37 ºC at 220 rpm. After 1.5 h, the OD 600 was measured every 15 min until the OD 600 level reached 0.45. The cells were transferred to cold 50 mL centrifuge tubes. Before spinning, the centrifuge was spun for a few seconds to reach 4 ºC. Then the cells were recovered by centrifugation at 1000 g for 10 min at 4 °C after which the medium was decanted from the cell pellets. The bacterial pellet was re-suspended in 50 mL of ice-cold solution containing 15 % glycerol with 75 mM of $CaCl_2$ and was incubated on ice for 5 min and then centrifuged at 1000 g for 10 min. After centrifugation, the cells were re-suspended in 2 mL of 75 mM $CaCl_2$ with 15 % glycerol solution. 100 µL aliquots were snap frozen in liquid nitrogen and stored in -80 °C freezer.

4.6   Macroscale (co-) Transformation Experiments

Competent *E.coli* cells were thawed on ice for 10 min and then 100 ng/µL of pFAB4876 or pSB1C3 DNA were added to 100 µL of competent cells in a 2 mL centrifuge tube. For co-transformation experiments, both plasmids were simultaneously added to the competent cells. After adding the DNA to the cells, the solution was gently mixed by flicking the bottom of the tube and incubated on ice for 15 min before heat shock. The heat shock transformation protocol

consisted of four steps (Figure 4.6): (1) the solution was placed in a water bath for 60 s at 42 ºC, (2) the solution was then placed on ice for 3 min, (3) 1 mL of fresh LB was added to the tube and then placed in a 37 ºC incubator for 1 h with shaking at 220 rpm, and (4) after recovery, the solution was added into a LB agar plate with ampicillin resistance and incubated 37 ºC overnight for colony growth. Colonies were manually counted, and transformation efficiencies were calculated by dividing the number of colonies counted on the plate by the total amount of DNA transformed expressed in µg.
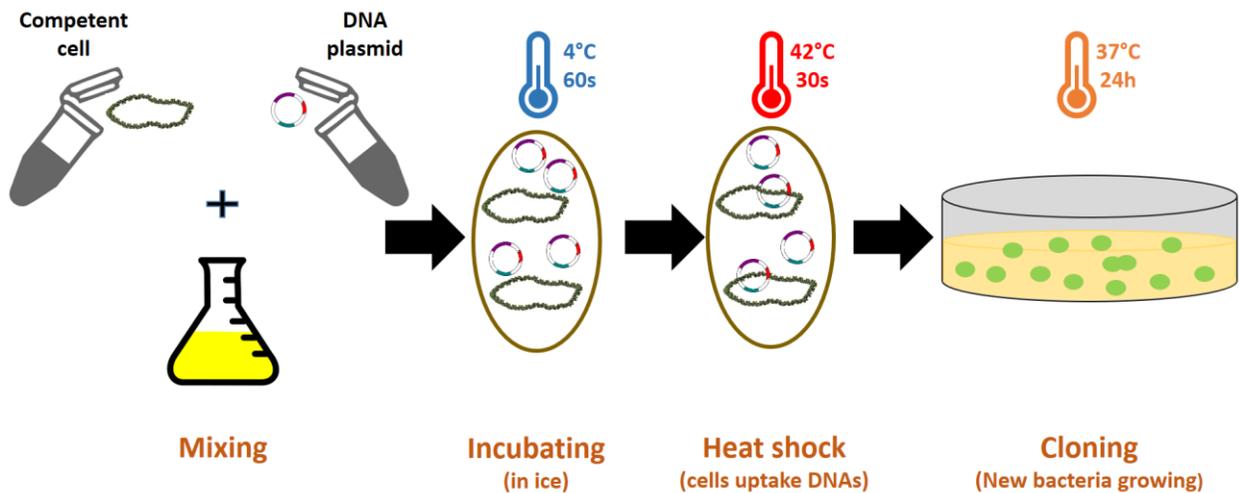

Figure 4.6 – Bacteria transformation protocol.

The protocol consists of mixing chemically competent bacterial cells with plasmid DNA. The mixture is left on ice and then heated to 42 °C for 30 s, then fresh media is added, and the solution is recovered in 37 °C for an hour before being plated on solid agar media with antibiotic selection overnight.

4.7　　Microscale Bacterial (co-) Transformation

Prior to the experiment, the competent *E.coli* cells were thawed on ice for 10 min. Plasmid DNA (pFAB4876 and pSB1C3) was diluted to a concentration of 1 μg/μl. $CaCl_2$ stock was prepared at 150 mM to maintain final concentration of transformation solution on chip at 75 mM of $CaCl_2$. For on-chip transformation, two thermoelectric modules were attached to the bottom of the DMF chip that provided two controllable thermal zones (4 ºC and 42 ºC – Figure 4.7) and all reagents were initially pipetted to the cold region on the chip.

For ITO-DMF configurations, 7 μL of each reagent including competent cells, DNA and $CaCl_2$ was pipetted into corresponding reservoir (see Figure 4.8a for device layout). A premade sequence code which was using our in-house software was executed to apply a voltage of 162 V_{rms} at 15 kHz frequency to dispense a 1 μL droplet from the reservoir. Three dispensed droplets (1 μL each) containing the DNA plasmid, *E.coli* cells in LB media and $CaCl_2$ were merged together on the chip in a 1:1:1 ratio. After merging and mixing, a heat shock protocol was applied which consisted of 60 s at 42 ºC followed by 3 min at 4 °C. The solution was taken out by pipette and placed into a micro centrifuge tube. 100 μL of fresh LB were added to the mixture and then the tube was placed at the incubator at 37 °C, 220 rpm for 1 h recovery. The transformed cells were plated on an agar plate with kanamycin antibiotic selection overnight. Three replicates were conducted in parallel on the same device.

For ITO-well-DMF configuration, 400 μL of cells were added to the 3D printed well (instead of directly in a reservoir) and 7 μL of the DNA plasmid and $CaCl_2$ were added directly to the reservoirs on chip. The procedures followed the ITO-well transformation protocol with the addition of refilling the main reservoir containing the cells. To refill the reservoir, the solution

containing cells were delivered to the ancillary reservoir by twisting the plunger through the hole on ITO top plate. Next, the fluid was actuated from ancillary reservoir until a liquid neck is combined with the liquid in the main reservoir. After the main reservoir was filled to the desired volume (~7 μL), which was measured by the impedance circuit, a splitting step occurred to break off the liquid neck. This were performed for three replicate measurements.
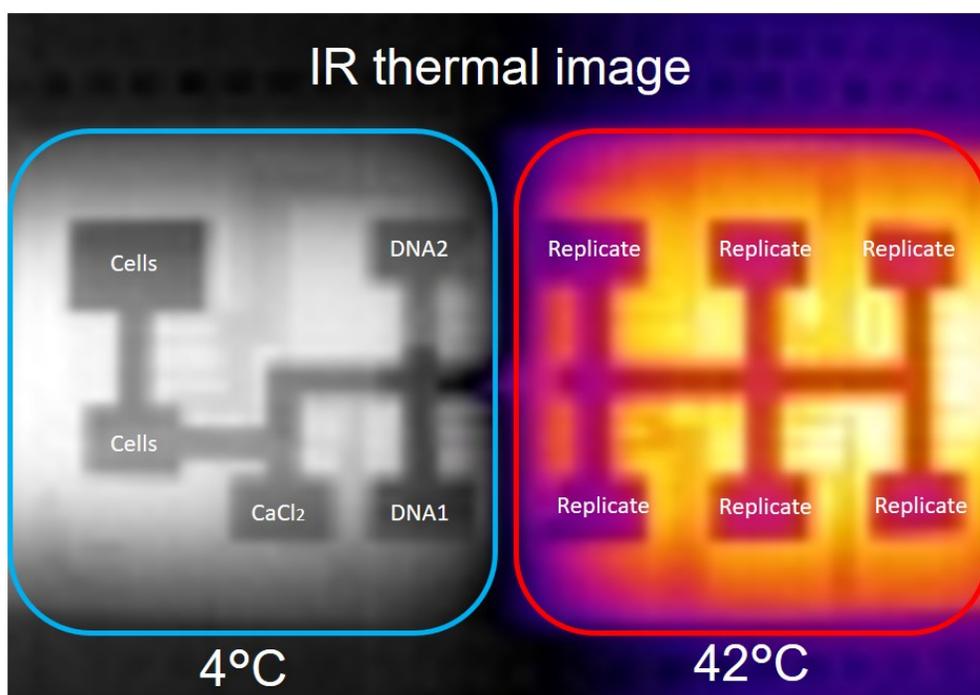

Figure 4.7 – Infrared images on the DMF device showing two temperature regions.

Two temperatures (4 °C and 42 °C) were used to enable bacterial transformation protocol on the device. Labels on the device show which reagent is stored on that electrode.

4.8   Enzymatic Assay

The endoglucanase enzyme assay was carried out on the two configurations ITO-DMF and ITO-well-DMF, and repeated at room temperature and 30 °C. For the 30 °C condition, the TEM was integrated below the assay areas and a closed-loop PID control was enabled for both configurations to maintain a steady-state temperature. On the ITO-DMF configuration, a unit droplet of enzyme solution (~1 μL) was dispensed into three assay areas on the device (see Figure 4.8b for the device layout) using a starting voltage of 162 V_{RMS} at 15 kHz. A substrate solution containing 40 μM 4-methylumbelliferyl β-D-cellobioside (MUC) in buffer (50 mM sodium-phosphate, pH 7.0) was dispensed from the reservoir and stored adjacent to an assay area. A second unit droplet of substrate solution was dispensed and serially diluted to 20 and 10 μM MUC droplets with buffer solution by mixing and splitting operations. The two final droplets containing 20 and 10 μM MUC were then stored adjacent to an assay area. To start the reaction, all three substrate droplets were simultaneously mixed with the enzyme droplets in the assay areas (and the TEM was activated, if required). After 30 minutes of incubation, a unit droplet of quenching solution (0.3 M glycine-NaOH, pH 11.0) was mixed with each mixed droplet containing enzyme and substrate solution in the assay area. On the ITO-well-DMF configuration, the same droplet operations were carried out, except that the well was used to replenish the main enzyme reservoir after dispensing an unit droplet of enzyme. After the assay, the device was placed on a well-plate and into a CLARIOStar plate reader (BGM Labtech, Ortenberg, Germany) to measure 4-methylumbelliferone (MUF) fluorescence at 449 nm with 368 nm excitation. The fluorescence intensity was measured by using the well-scanning function (scan matrix = 15x15, scan diameter = 6 mm, focal height = 4.0 mm and gain = 1180), and the maximum fluorescence intensity value for each droplet was recorded

for analysis. Each assay was repeated three times. All solutions used on the device contained 0.05% F-68 Pluronics additive.
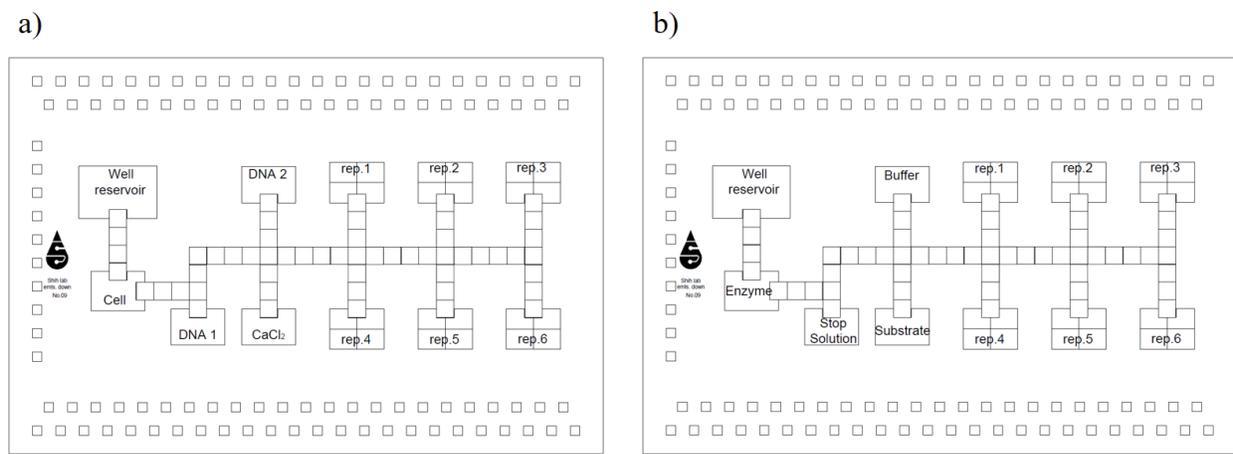
Figure 4.8 – DMF device layout for the world-to-chip validation study.

a) Bacterial transformation device layout and b) Enzymatic assay device layout with the respective reagents used in each study.

4.9   Cloning and Protein Expression

The sequence for the *Rhodothermus marinus SG0.5JP17-172* endoglucanase gene (EGL) was obtained from NCBI (GenBank accession number WP_014065767.1) and was synthesized by IDT (Coralville, IA) as a linear DNA fragment. The gene was amplified by PCR using Phusion polymerase (Thermo Fisher scientific, Waltham, MA) according to manufacturer's instructions. The following primers were used to introduce a 5' XbaI and a 3' BamHI restrictions sites:

Forward:

5'- TGACTGACTCTAGAAATAATTTTGTTTAACTTTAAGAAGGAGATATACC ATGCGTGTATTGGCGCTGC - 3'

Reverse:

5' - GCATGCATGGATCCCTAATTGCGTGGATTTAATTGGCGC - 3'

The PCR product was purified, digested with XbaI and BamHI for two hours, and ligated into a linearized pET16b vector. The ligation product was transformed into chemically competent *E.coli* DH5α cells and plated on selective media. Single colonies were inoculated in 5 mL of LB media containing 100 µg/mL ampicillin overnight and plasmids were extracted using a BioBasic miniprep kit. Proper insertion of the gene was verified by digesting 2 µg of plasmid with XbaI and BamHI checking proper insert size on a 0.8% agarose gel. The cloned plasmid (pET_EGL) was transformed into E.coli BL21(DE3) for protein expression. The transformed cells were inoculated overnight in a 5 mL pre-culture. The next day, a 100 mL starter culture of low optical density (OD) was generated by diluting the overnight culture and grown at 37 °C with 200 rpm shaking. Upon reaching OD 0.4, expression of the EGL gene was induced by addition of 1 mM IPTG for 6 hours. The final induced culture was divided into 40 mL aliquots and centrifuged at 4000 rpm for 5 min. The pellets were frozen and kept at -20 °C for later used. Thawed pellets were lysed at 4 °C for 15 min by resuspending in 10 mL of lysis solution comprising 1 mg/mL lysozyme, 25 U/ml benzonase and 1 mM phenylmethanesulfonylfluoride (PMSF). The lysates were centrifuged again at 4000 rpm for 5 min to collect the protein pellets. The pellets were resuspended in 10 mL of assay buffer (50 mM sodium-phosphate, pH 7.0) and diluted 50-fold in the same buffer before use.

Chapter 5.   Results and Discussion

This chapter describes my results in validating the world-to-chip interface platform. I will describe the device design optimization, the validation of the platform for integrated reagent delivery system and on-chip temperature control system. Also details the process of applying our platform on two biological application including bacteria transformation and enzymatic assay.

We have integrated two world-to-chip interfaces for digital microfluidics, namely, integrating reagent delivery and refilling and temperature control. The new system, as shown in Figure 5.1a, was formed by 3D printing a bottom holder to interface a 50 x 75 mm device, thermoelectric module (i.e. Peltier), temperature sensor, and the aluminum block to house a temperature sensor. A top 3D printed cover (shown in blue) is mated to the bottom holder with four fitting screws (show in white) and sandwiches the pogopin holder (used to deliver electric potentials to the electrodes) and the device. The addition of the top cover with the fitting screws enabled tight contact of the pogopin board to the device.
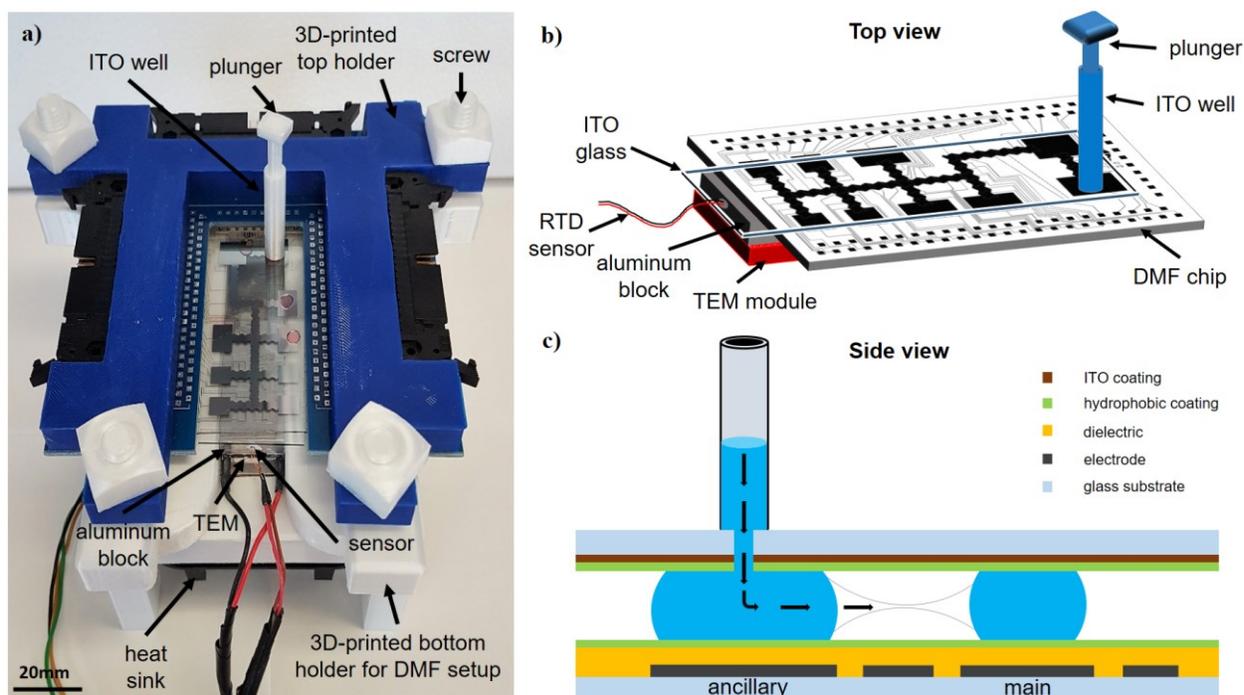
Figure 5.1 – World-to-chip interfaces for digital microfluidic devices.

Two world-to-chip interfaces (reagent delivery and temperature control) are combined with the digital microfluidic device for reagent delivery and closed-loop temperature control.

A top view of the device is shown in Figure 5.1b – as depicted, the digital microfluidic device consists of electrodes and each electrode is wired to a contact pad. This array of contact pads on the side of the device is connected to the pogopin board (which is connected to the automation system – see Figure 2.3). Devices were assembled with the top-plate (with or without well) and droplets are manipulated on the DMF device by applying an AC field between the electrodes on the top and bottom plates. Temperature control of the device is managed by the thermoelectric module (i.e. Peltier) which can be positioned underneath the device with a temperature sensor for closed-loop control. Both of these world-to-chip interfaces represent a

significant advance over the previous DMF device configurations which do not include a reagent delivery system or a closed-loop control scheme for temperature control.[78, 79]

5.1   Platform validation #1: Automated Reagent Delivery System

In digital microfluidic systems, reagent delivery has been alleviated by the addition of reservoirs on the device. Users typically manually pipette the reagents directly onto a reservoir and use automated sequences to dispense liquids from the reservoir [80]. However, as shown by some groups, [81, 82] dispensing from reservoirs is not reproducible process and dispensing have high variability in volumes. There are methods such as incorporating capacitative, [83, 84] or image-based feedback sensing,[56] or other droplet tracking methods, [85] to improve dispensing reproducibility but these are not capable of refilling the reservoir when it is depleted (i.e. there is a limited number of times that a droplet can be dispensed from a reservoir).

As shown in Figure 5.1c, the central feature of this design is a 3D printed cylindrical reagent well mated to the top of the ITO ground plate which contains a drilled-hole inlet. Using a reagent well, devices can hold larger volumes (~400 μL) than a typical reservoir (which hold ~1-10 μL) on the chip. We call this configuration 'ITO-well-DMF' and the well will be refilled by a plunger when the reservoir has been reduced in volume due to dispensing droplets. The design and alignment of the reagent well was optimized to address two challenges: consistent fluid refilling of the reservoir and enabling reproducible, equal-sized droplet dispensing from the reservoir. For these challenges, we observed that reliable refilling and reproducible dispensing required two reservoirs – which we label as main and ancillary reservoirs. In initial experiments, we observed that if the well was directly overlapping the main reservoir (Figure 5.2) or partial overlap as suggested from a previous study [86], the fluid from the well will not be confined to the

reservoir and spread elsewhere on the device. In this configuration, the main reservoir would frequently be overfilled (> 7 μL) which caused significant difficulties in dispensing droplets. A motorized component to automatically deliver the liquids would alleviate this [87] , but here we added an ancillary (i.e. secondary) reservoir to dispense droplets from this reservoir and is used to refill the main reservoir (Figure 5.4). We found with the addition of the ancillary reservoir facilitated easy refilling without any external motors or pumps. The process of reagent delivery follows three steps (Appendix Figure A.1): (1) the threaded plunger delivers liquid from the well to the ancillary reservoir on the chip, (2) a liquid neck is created from the ancillary to the main reservoir and the volume in the main reservoir is measured via impedance (Figure 4.3), and (3) when the volume reached a target of 7 μL (i.e. V_{read} = 12.9 V; Figure 5.5) in the main reservoir, the liquid neck is broken off by actuating the ancillary and main reservoir. With only the main reservoir (i.e. without an ancillary reservoir), significant amount of trial-and-error was required to obtain the target reservoir volume. The excess time required to refill the main reservoir at the target volume typically fouled the surface of device due to the trial-and-error process. With the ancillary reservoir, a systematic process is introduced (i.e. without trial-and-error) and this minimizes the biofouling on the surface of the device.
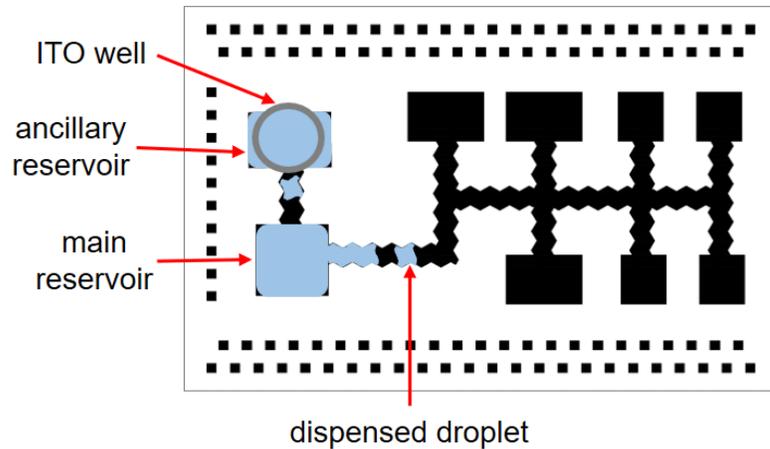
Figure 5.2 – DMF device for reagent delivery.

A DMF device showing the labeled reservoirs (ancillary and main) used for reagent delivery. The 3D printed well is aligned to the ancillary reservoir and fluid is delivered to this reservoir. An unit droplet is dispensed from the ancillary reservoir and is used to refill the main reservoir. This is repeated every time a droplet is dispensed from the main reservoir.

Figure 5.3 – Calibration curve to correlate volume and voltage.

A droplet of specific volume was manually dispensed on the reservoir and the electrode was actuated using 80 V_{rms}. The measured voltage (V_{read}) is the voltage drop across the resistor. This volume has a linear correlation with the voltage. Three replicates were used for each measurement.
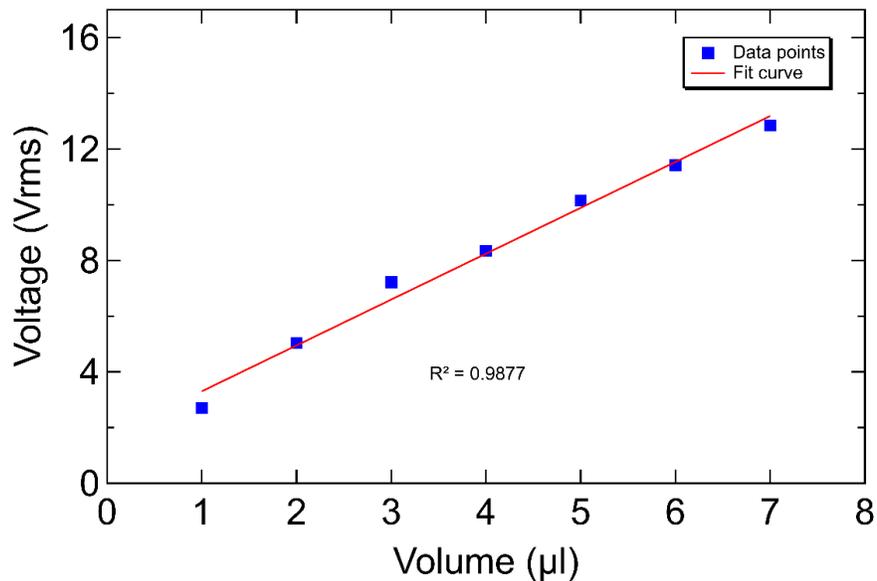
To test dispensing of liquids using the well, we tested three liquids that varied in viscosities. As shown in Figure 5.4, are six graphs showing the utility of the reagent well and the precision of dispensing using the ITO-well-DMF and ITO-DMF configuration for three types of liquids ranging in viscosity (LB media, water, and methanol). In the ITO-DMF configuration (Figure 5.4a-c), droplets are repeatedly dispensed from the main reservoir until it was not possible to dispense any more droplets. In our experiments, the maximum number of droplets dispensed with a reservoir volume of 7 µL is five droplets with a target volume of ~1 µL. In the ITO-well-DMF configuration (Figure 5.4d-f), a droplet is dispensed from the main reservoir and the reagent well refills the ancillary reservoir by dispensing a droplet to refill the main reservoir. Three key results are obtained from these graphs: (1) the ITO-well-DMF configuration (with reagent delivery) allowed continuous dispensing – in our experiments, we dispensed 10 droplets (compared to only 4-5 droplets without the well) and can be increased to more dispensed droplets. (2) The precision of the dispensed droplets in the ITO-well-DMF configuration (RSD = 11.07%, 17.28%, 15.58% for LB, water, methanol respectively) was higher than the precision in the ITO-DMF configuration (RSD = 16.10%, 38.90%, 38.88% for LB, water, methanol respectively) which demonstrates the reproducibility of using the reagent well. (3) The precision of the dispensed volume is highly dependent on the reservoir volume. There are a number of factors that suggest that there is a fundamental change occurring on the device (e.g., dielectric degradation, contact angle saturation) that can change the dispensed droplet volume.[81] These are inevitable changes on the device and

having a refilling reservoir is the optimal solution for refilling and ensuring reproducible dispensed droplets.
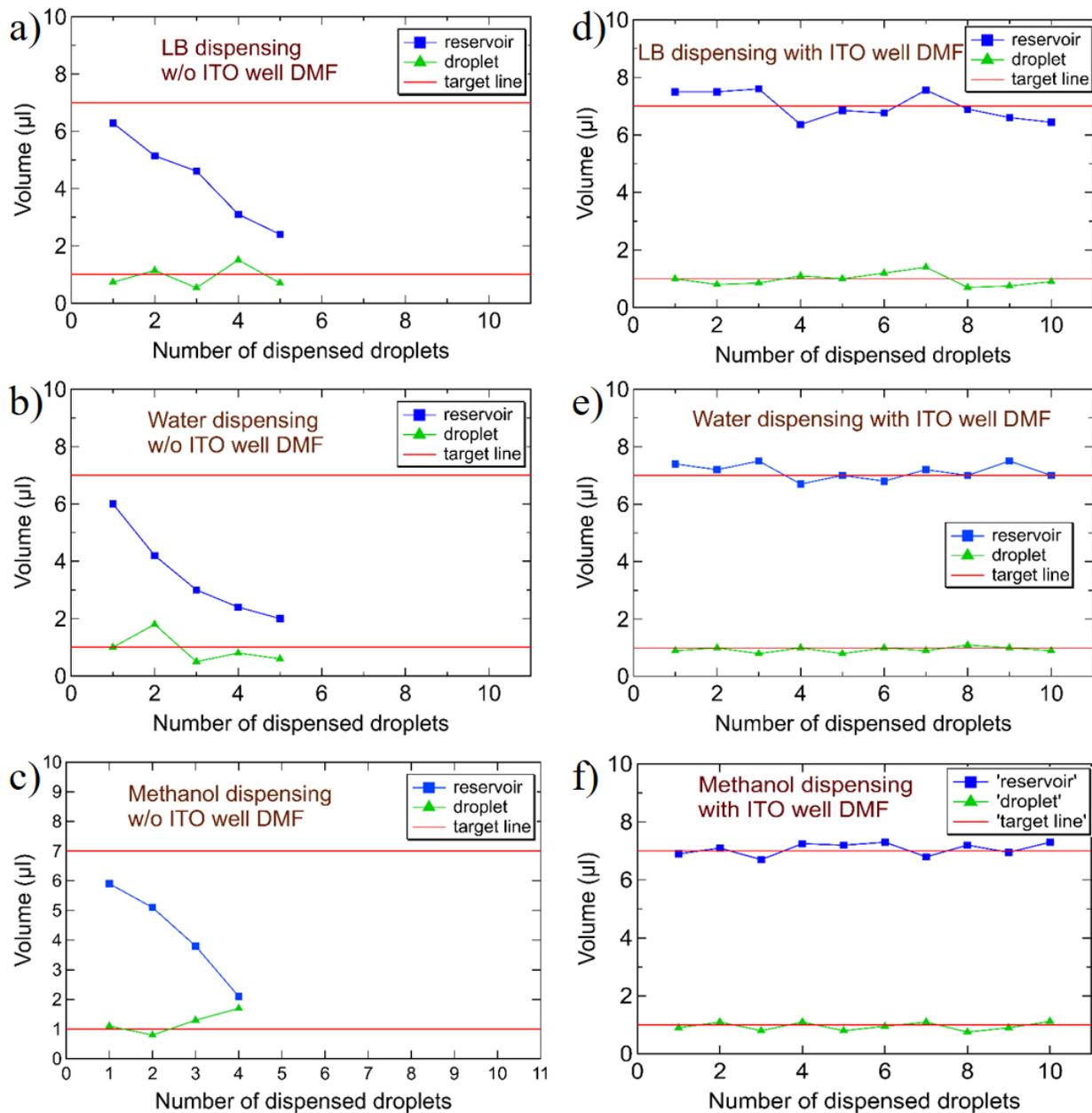

Figure 5.4 – Effects of ITO-well-DMF configuration on droplet dispensing.

(a-c) correspond to volumes measured (via impedance) after dispensing droplets without the 3D printed well for LB media, water, and methanol respectively. (d-f) correspond to volumes

measured (via impedance) after dispensing droplets with the 3D printed well for LB media, water,
and methanol respectively.

5.2   Platform validation #2: Integrated Temperature Control

A second world-to-chip interface that is important for microfluidics is the control of temperature. There are numerous papers that have discussed the integration of micro-heaters (i.e. Peltier elements) to establish a uniform or gradient temperature in a given region on a microfluidic device.[71-75] However, in these microfluidic studies, the parameters used for the Peltier are optimized for their own biological or chemical application. There has not been a fully modeled and characterized Peltier control system that allows for quick analysis, design and optimization. In fact, a significant amount of trial-and-error is required to optimize the control-loop parameters and design. A model that can optimize the thermoelectric module can reduce the time for the design cycle and quickly find parameters suitable for their own applications. Furthermore, it can also help validate and understand the experimental results. As shown in Figure 5.5, is the block diagram that we used to simulate the closed-loop thermoelectric system. A temperature set point is the input and subtracted from the sensor-read temperature on the Peltier and the error is the input to the PID controller. The PID controller uses this input and tune the system by tuning three constants K_p, K_i, and K_d for proportional, integral, and derivative control respectively. This output is connected to the plant which is the thermoelectric module and is thermodynamically modeled by two main effects: thermal and Peltier. (see Appendix for detailed description of the thermal plant).
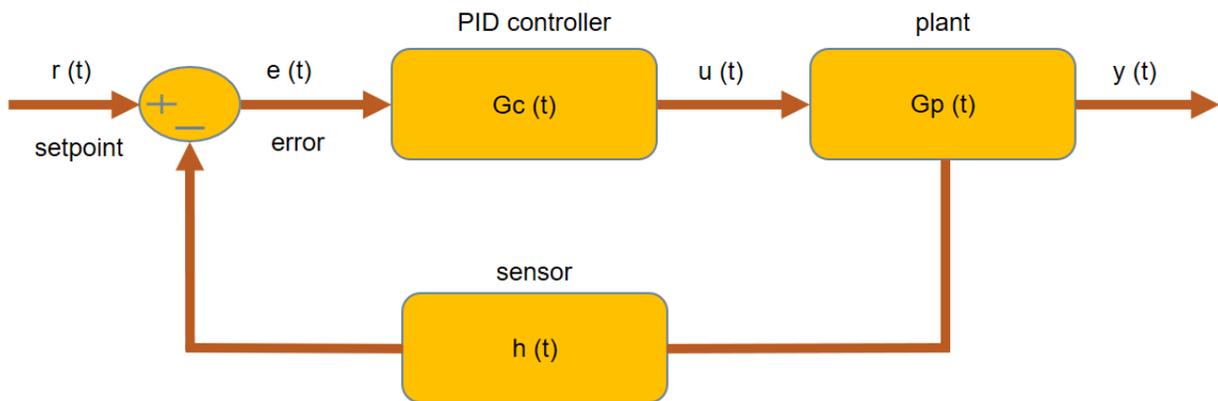
Figure 5.5 – Closed-loop temperature control system.

A block diagram showing the modeled PID controller along with the plant (which is the thermoelectric module) and a temperature sensor. In this model, the PID controller tunes the system by optimizing the error input [e(t)]. Parameters used this simulation are shown in Table 4.1.

The output of the plant is read by the temperature sensor and returned to the input. As a first test of this model, we chose three different scenarios to numerically simulate the target temperature of 42 °C (Figure 5.6 and Figure 5.7). In these scenarios, we chose to verify the robustness, optimality, stability, and accuracy of the proposed controller with the modelled plant. Using parameters $K_p = 15$, $K_i = 1.2$, and $K_d = 0.5$ (Figure 5.7) shows the most optimal result – i.e. fast rise time, low fluctuation, and high stability at the target temperature of 42 °C.

Figure 5.6 – Effects of closed-loop temperature control with non-optimal control parameters.

a) A graph shows the temperature output when the system is given a low rise time, high fluctuation, and low stability. b) A graph shows the temperature output when the system is given a low rise time, high overshoot, and no stability. All experiments had a target temperature of 42 °C.
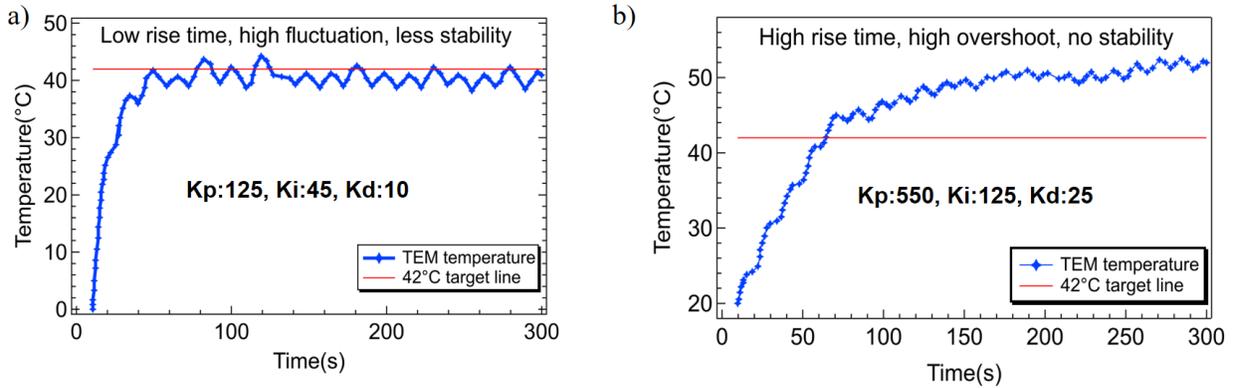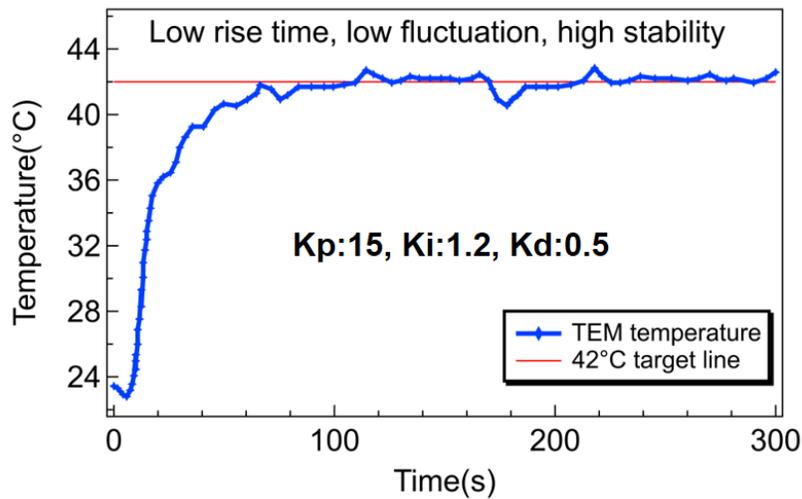

Figure 5.7 – Effects of closed-loop temperature control with optimal control parameters.

A graph shows the temperature output when the system is given a low rise time, low fluctuation, and high stability.

Table 5.1 – The effect of increasing each of the parameters

Parameter	Rise time	Overshoot	Settling time	Steady-state error	Stability
K_p	Decrease	Increase	Small change	Decrease	Degrade
K_i	Decrease	Increase	Increase	Eliminate	Degrade
K_d	Minor change	Decrease	Decrease	No effect in theory	Improve if K_d small

The simulated shows that parameters K_p and K_i are sensitive to changing the stability and overshoot of the target. This is expected since increasing the proportional gain (K_p) will have the effect of reducing the rise time while the steady state error can be eliminated by introducing some element of integral control (K_i). Given the simplicity of our model, this will allow users who are not familiar with control theory to implement closed-loop temperature control and integrate with reagent delivery control for digital microfluidics.

5.3   Application #1: Bacterial Transformation

To evaluate the functionality of the world-to-chip interface we conducted a bacterial transformation study on the digital microfluidic device. Bacterial transformation typically involves the insertion of plasmid DNA (Figure 5.8) into *E.coli* (or some microbe) using a heat shock (or electric-field) based method. These traditional methods have been used to express new genetic information using a plasmid system such that it can enable an understanding how the gene-encoded protein functions and interacts with other proteins inside the cell. There has been much interest in automating the transformation procedure using digital microfluidics (or a derivative thereof) [88, 89] since fields like synthetic biology typically requires the optimization of metabolic

pathways [90] or logic gated systems [91] which consists of many genetic elements that be difficult to manipulate if manually performed. Here, we have followed these studies with added features of closed-loop heat and cooling control and reagent delivery that is not present in these studies.
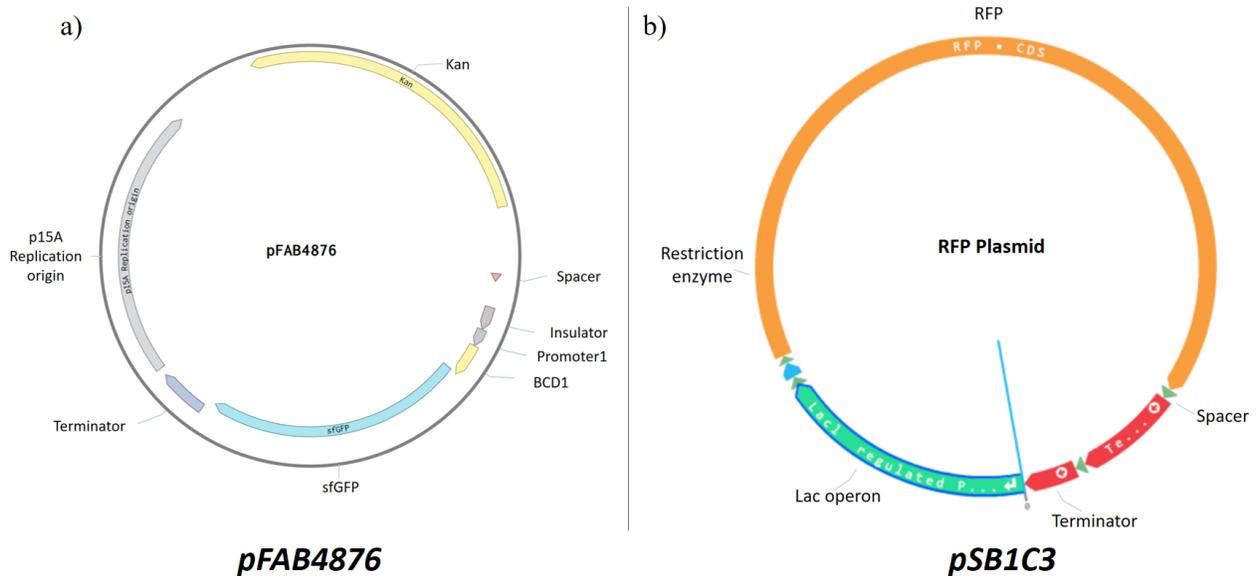
Figure 5.8 – Plasmid maps

a) pFAB4876 and b) pSB1C3 used for bacterial transformation. Each plasmid map consists of a promoter, ribosomal binding site, the gene of interest (e.g., GFP, RFP), and a terminator. An origin of replication along with an antibiotic resistance marker were included for DNA replication and for selection on agar plates respectively.

To perform transformation with our integrated world-to-chip interface, we designed a microfluidic device (Figure 5.9) that is capable of transformation by heat-shock. The device consists of four reservoirs that holds droplets of bacteria cells, LB media, $CaCl_2$ solution, or the plasmid coding for eGFP.

Figure 5.9 – Digital microfluidic device used for bacterial transformation.

This device is used for implementing the bacterial transformation protocol (see Appendix Figure A.1). Two key features w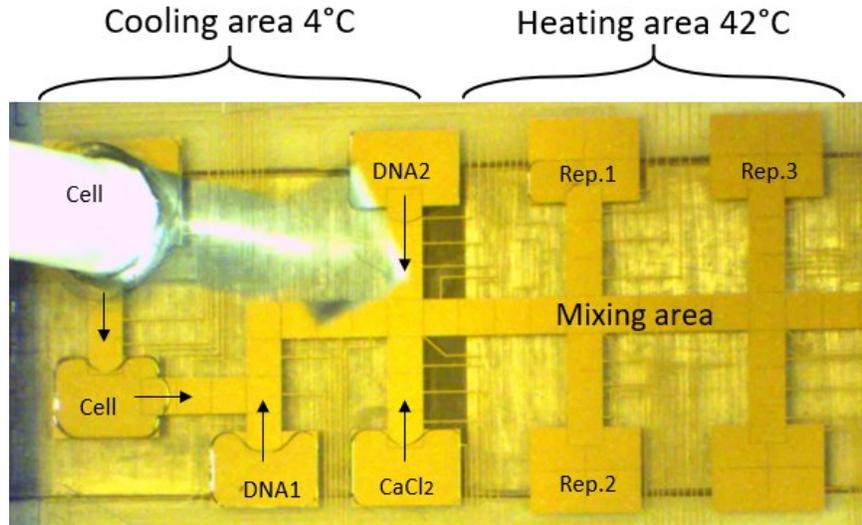ith this device is the addition of two world-to-chip interfaces: 1) 3D printed well that is used for delivering cells in media and 2) two Peltier elements (below the device) that is used to keep temperatures at 4 °C and 42 °C.

Two new features (compared to other DMF and transformation studies) were added to this configuration – (1) a 3D printed well that is used for automated reagent delivery without the manually refilling of the reservoirs and (2) the closed-loop PID control of the Peltier. Since most reagents only required one time dispensing, we used the 3D well for cells since it required more frequent dispensing. We also integrated the Peltier module below our DMF device below our DMF device to provide a region with controllable thermal zone. Since heat-shock transformation protocols require different temperatures (4 °C, 37 °C, and 42 °C), we first tested the controllability of the Peltier module. We implemented an experiment to determine if the module is capable of reaching the desired temperatures. As shown in Figure 5.10 are the temperature curves for the open- and closed- loop control system integrated with the Peltier modules. In the open loop

control, the Peltier modules were not capable on reaching the desired temperatures within the set time of 1 min for each set temperature (4 °C and 42 °C). However, with the closed loop PID control system, we observe that temperatures can quickly rise to 42 °C at a rate of 2.1 °C/s and can drop the temperature to cold temperature at a rate of 1.01 °C/s. We also used our simulated model to verify and to understand our experimental results. The experimental results showed a good match to the simulated model. One key difference is faster temperature decay rate in the experimental compared to the simulation. We hypothesize that the difference is due to integrating a fan with the Peltier (which was not part of the simulation model) since it provides excellent heat dissipation. Overall, the closed loop PID system is important since having temperature control can significantly increase the uptake of DNA in bacteria.[92, 93]
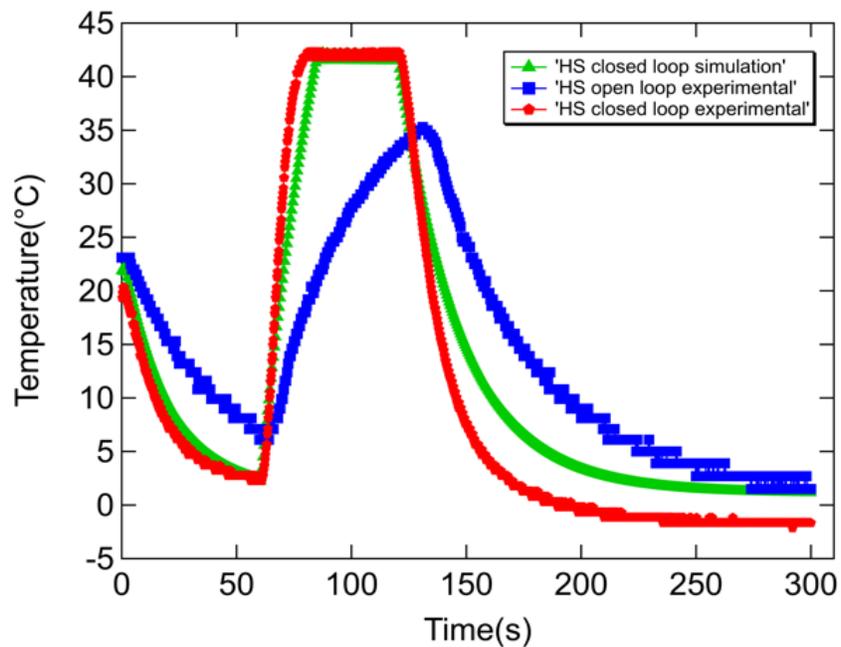

Figure 5.10 – The output temperature curve for open- and closed-loop control.

Open-loop control (shown in black) has slower ramping constant and a slow decay rate. Closed-loop control (shown in red) has faster ramping constant to 42 °C and fast decay rate towards 4 °C. Closed-loop control experiment was verified via simulation (shown in green).

Next, we tested our closed-loop control system by experimentally transforming chemically competent *E.coli* cells (*DH5α*) with a GFP expression plasmid (pFAB4876) on the device. As shown in Figure 5.11, the transformation efficiency in three scenarios are compared. First, the experiment was done without having any kind of control. Then we added PID closed loop control which is second experiment and lastly, we added ITO-well to the chip. With PID control Peltier module, we were able to obtain efficiencies of 2.03×10^4 colonies forming units per μg of DNA (CFU/μg). This was significantly (P = 0.041 at 95% confidence) higher than the open-loop controlled transformation (3.67×10^3 CFU/μg).

Figure 5.11 – Transformation efficiency showing the effects of two world-to-chip interfaces.

The experiment with reagent delivery with closed-loop temperature control achieved higher transformation efficiencies than the cases with only closed-loop control and no control.

As expected, the temperature control for on-chip transformation has a significant effect on the transformation efficiencies (as observed in other studies). In addition, we hypothesized that with that the reagent well delivery system would be useful to dispense droplets at more precise volumes which will improve transformation efficiencies. The data validated our hypothesis – for example, in three trials of conducting bacterial transformation on-chip using the reagent delivery system and with closed loop control improved the transformation by ~7-fold (1.48×10^5 CFU/µg, p = 0.007) compared to the closed-loop control and with usual dispensing techniques (i.e. no refilling the reservoir after one dispensing action). A possible explanation for this increase is that variable dispensing volumes can create variability in final DNA concentrations, pH of the solution, $CaCl_2$ treatment, and nutrient concentration in which all of these factors can affect overall transformation efficiencies [94-97].

We also measured the efficiencies for injecting two DNA plasmids (i.e. co-transformation) to determine if the ITO-well-DMF configuration can increase efficiencies for a typical low efficient process as shown in Figure 5.12. In addition, we were motivated by the wide-spread interest in applications like gene-editing [98] or metabolic engineering [99] that require transformation of multiple plasmids for the expression of multiple genes. In this experiment, we hypothesized that similar trends would be observed for these experiments compared to a single transformation.
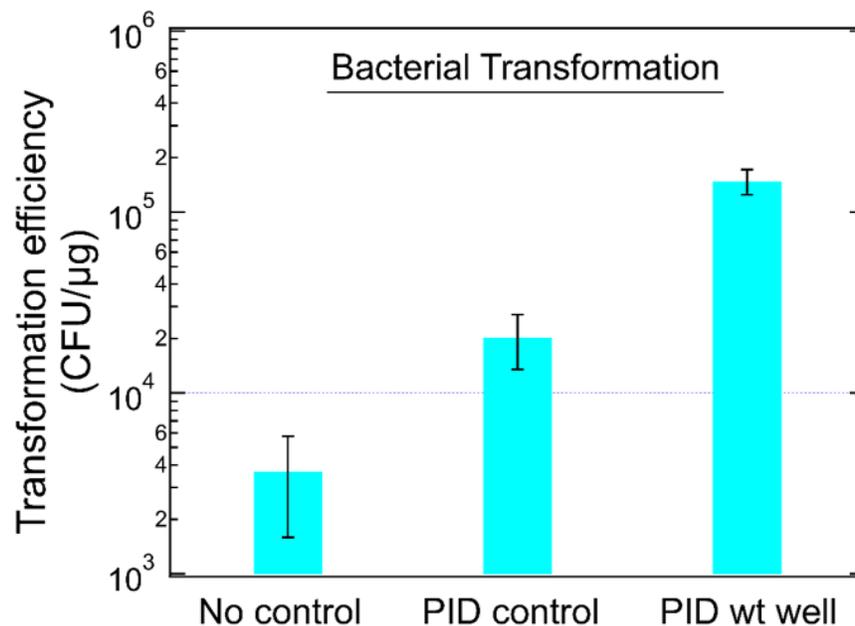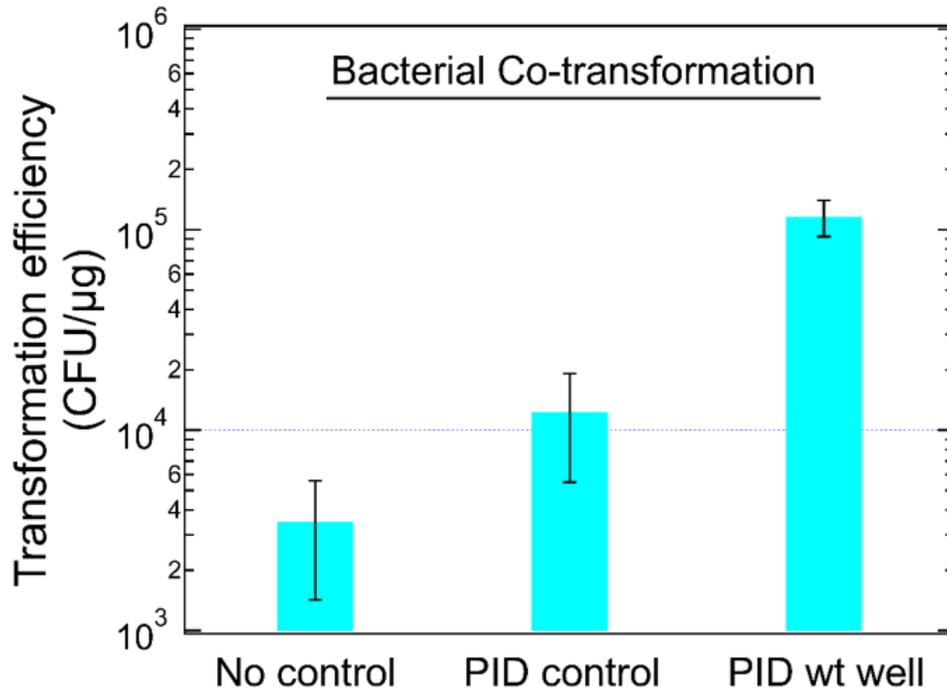
Figure 5.12 – Co-transformation efficiency showing the effects of two world to chip interfaces.

The experiment with reagent delivery with closed-loop temperature control achieved higher transformation efficiencies than the cases with only closed-loop control and no control.

As shown, the trends confirm to be similar such that the integration of both world-to-chip interfaces improved the efficiencies and the differences are significant ($p = 0.001$). We also qualitatively evaluated the colonies (Figure 5.13) and each colony expressed the GFP and the RFP plasmid verifying that each bacteria colony has uptake the two plasmids. Overall, we have demonstrated the need for the world-to-chip interfaces for digital microfluidics and propose that method described here would be uniquely suited for future experiments involving bacterial transformation.

Figure 5.13 – Colony forming units.

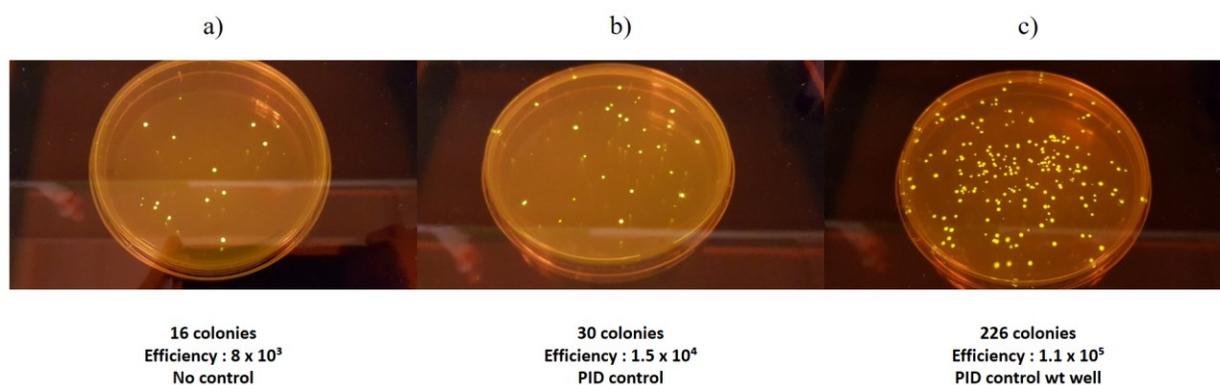*In the control case (a), on average 16 colonies were formed on the plate with antibiotic selection. With closed-loop control (b), an increase in number of colonies were observed (~30 colonies). The highest number of colonies (~226 colonies) were observed when both world-to-chip interfaces were added to the device for bacterial transformation.*

5.4   Application #2: Enzymatic Assays

As a second demonstration of an application for our world-to-chip interface integrated with digital microfluidics, we explored the implementation of enzymatic assays. Enzymatic assays are often used to measure the activity of produced proteins and are vital to understanding enzyme kinetics and inhibition. The enzyme kinetics provides crucial information on the mechanism of the enzyme and on the interactions of the enzymes with substrates, inhibitors, drugs, etc…. One of the fundamental applications of DMF is the implementation of enzymatic reactions [56, 100-103]. The protocol typically consists of precise metering of reactants by dispensing droplets from reservoirs and merging and mixing to create a droplet that represents the microreactor. The microreactors on the DMF device are typically analyzed using integrated in-line detectors [76, 104,]

[105] or with offline detectors (e.g., fluorescence-based plate readers) [60, 106, 107]. However, most enzymatic assays conducted on DMF are either performed at room temperature or without refilling of reservoirs for dispensing droplets [100]. These corresponding factors give rise to two limitations: (1) prevents the study of most industrial-based enzymes which are active at higher temperatures (> 25 °C) and (2) prevents the study of different conditions on the device that requires droplets (containing substrate enzyme, or buffer) to be dispensed multiple times. These limitations motivate the development of our world-to-chip for digital microfluidics for the implementation of enzymatic assays that require heating and testing of multiple conditions in parallel.

Here we report an enzymatic reaction that involves cellulase-based enzymes that are involved in the degradation of biomass into sugar that are useful for biofuel production [108]. Specifically, we tested an endoglucanase (which are optimal at higher temperatures) from *Rhodothermus marinus SG0.5JP17-172* that is typically used to catalyze the hydrolysis of the (1,4)-glycosidic bonds [109]. Droplets containing the 4-methylumbelliferyl β-D-cellobioside (MUC; substrate) and the endoglucanase enzyme were mixed and incubated for 30 min using the same DMF device as described previously. After incubating, the droplets were analyzed via fluorescence. Figure 5.14 shows the chemical scheme of the assay which consists of using MUC in which the endoglucanase cleaves the β-(1,4) bond to give a cellobiose and a methylbelliferone fluorescence product.
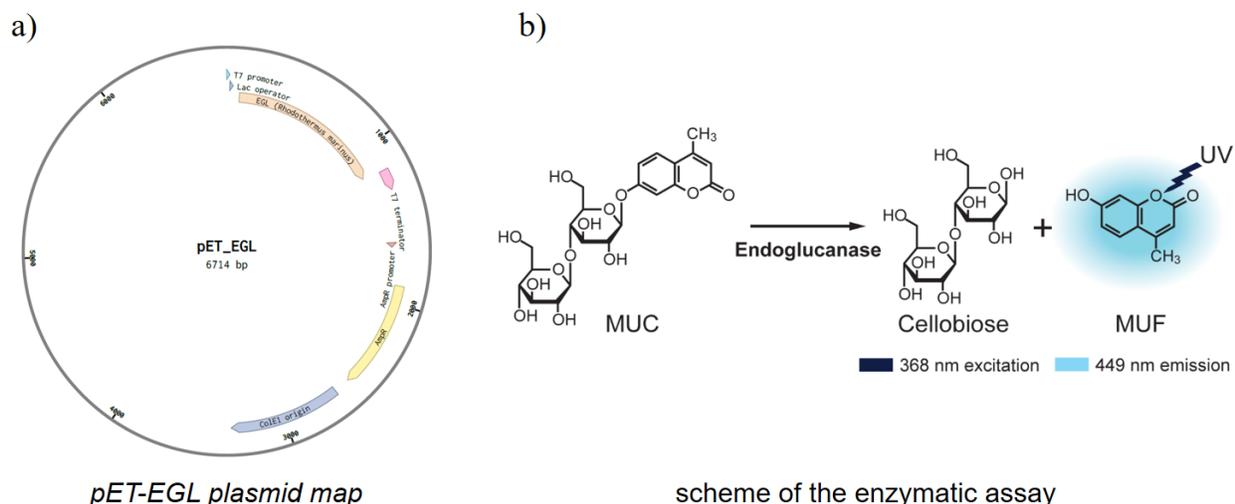
a) pET-EGL plasmid map

b) scheme of the enzymatic assay

Figure 5.14 – Enzymatic assay.

a) The plasmid used for the EGL enzymatic assay. b) The chemical scheme for the enzymatic assay. The 4-methylumbelliferyl β-D-cellobioside (MUC) was mixed with an endoglucanase to produce cellobiose and a fluorescent product (MUF). This fluorescent product is correlated to the activity of the enzyme (i.e. higher fluorescence, higher activity of the enzyme).

Using this chemical scheme, we tested the enzymatic activity of the endoglucanase using the 3D printed well for refilling of the reservoirs on the device to enable reproducible droplet dispensing of the enzyme and the closed-loop Peltier module to perform the assay at elevated temperatures (30 °C). As shown in Figure 5.16, the fluorescence output (i.e. the measure for enzyme activity) was plotted as a function of three substrate concentrations (5, 10, 20 µM) at two temperatures (23 °C and 30 °C). As expected, the key trend is reproduced, higher temperature lead to higher output fluorescence compared to room temperature experiments.

Figure 5.15 – Effects of temperature on the enzymatic assay.

This graph shows the fluorescence intensity (i.e. the MUF product) as a function of substrate concentration at two temperatures 23 °C and 30 °C. Fluorescence measurement was taken after 30 min incubation with the substrate. Each experiment consisted of at least three trials and the error bars represent ±1 s.d.

In a second assay, we performed the enzymatic assay with and without the reagent delivery system and with the closed-loop Peltier system set to 30 °C. Figure 5.17 shows the fluorescence output for each substrate concentration with and without the reagent delivery system. As shown, the fluorescence was significantly higher (ANOVA two-way test, $P < 0.05$) for experiments with the reagent delivery system. A potential cause for this difference between the data is changes in the droplet volumes. There are studies that show small changes in volume can lead to changes in

the pH, salt and detergent concentrations which can reduce the activity and stability of thermophilic enzymes by 20-30 % [110, 111]. In the future, given the widespread interest of automating enzymatic assays on DMF, we propose that the world-to-chip techniques reported here, in which reagent delivery and refilling and integration of heating will be useful for other types of enzymatic-based assays.

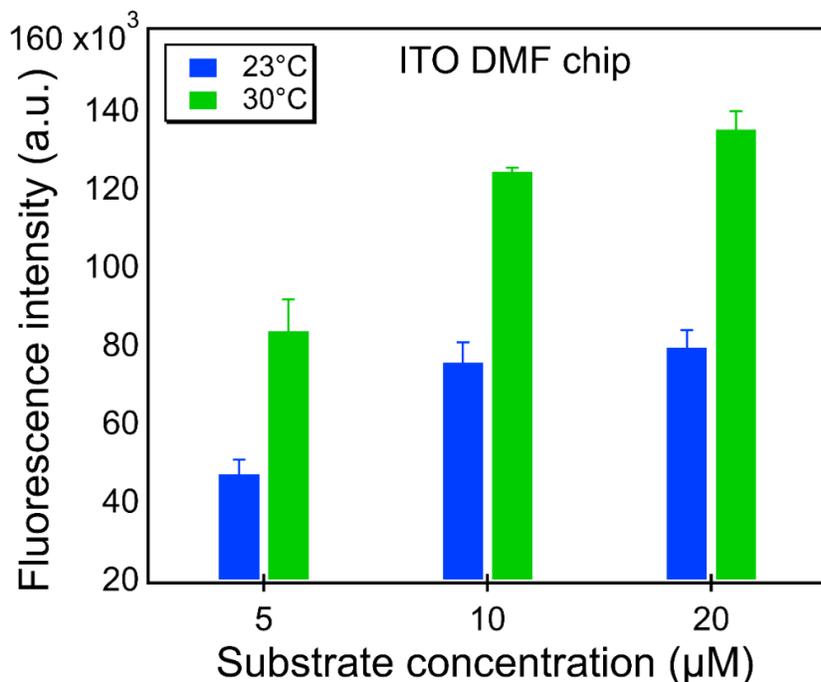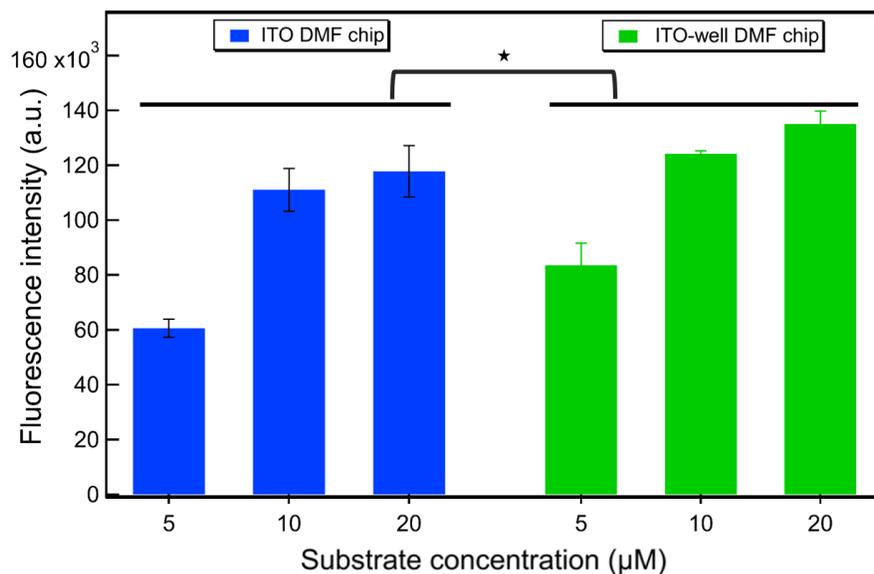**Figure 5.16** – **Effects of integrating the reagent well on the enzymatic assay.** *This graph shows the fluorescence intensity (i.e. the MUF product) as a function of substrate concentration for two 30 °C. Fluorescence measurement was taken after 30 min incubation with the substrate. Each experiment consisted of at least three trials and the error bars represent ±1 s.d.*

Chapter 6.   Concluding Remarks and a Look to the Future

In this section, I recapitulate the hallmarks of the thesis and review the merits of the world-to-chip interface platform as a versatile digital microfluidics platform. In addition, I evaluate the future work related to the world-to-chip interface platform.

6.1   Conclusion

We have developed two world-to-chip interfaces, namely a reagent delivery system and a closed-loop heating/cooling module, for digital microfluidic systems. The reagent delivery system consists of a 3D printed well integrated to the top-plate of the DMF system. The reagent well is equipped with a plunger that uses pressure to deliver and to refill the reservoirs on the DMF device. We also incorporated a closed-loop thermal/cooling Peltier module to control the temperature on the device. To understand and to verify the experimental results, we created a PID and Peltier model to simulate the temperatures on the device. We applied our world-to-chip interfaces to two widely adopted applications: bacterial transformation and enzymatic assays. Both applications show the requirement for world-to-chip interfaces and demonstrate the potential in moving towards a customizable and automated benchtop microfluidic system.

6.2   Future Perspectives

The demand for using digital microfluidics-based biochips are increasing in number. To elevate this technology to the next level, many aspects of DMF must be advanced at the same time such as throughout, controllability, ease of integration, and interfacing. Moreover, it is expected

that these microfluidic biochips will be integrated with microelectronic components in next-generation system-on-chip (SOC) designs [112].

As described in this thesis, we developed a prototype for integrating the digital microfluidics to other components to facile the performance. As a proof of principle, this work showed a promising platform for world-to-chip interface for digital microfluidics to achieve higher reproducibility and more controllability over the experiments. One possible area for further research is to expand the range of volumes (pL, nL, mL) that can be dispensed and delivered.

In addition, digital microfluidics has often been limited by its throughput. The number of assays which can be executed in parallel on a DMF chip is often referred as throughput. There have been many studies that has improved the throughput on DMF devices. [103, 113] Therefore, the world-to-chip interface also requires improvement in terms of throughput. A possible solution is to have a 3D printed ITO-well with an increased number of wells or create injection molded cartridges that contains several wells for reagent storage.

References

1.   Takatsy, G. The use of spiral loops in serological and virological micro-methods. *Acta. Microbiol. Acad. Sci. Hung.* **3**, 191-202 (1955).

2.   Einstein, A. Investigations on the theory of brownian movement. *Dover Publications* (1956).

3.   Berg, H. (Princeton University Press; 1993).

4.   Taylor, G. Dispersion of soluble matter in solvent flowing slowly through a tube. *Proc. R. Soc. Lond. A Math. Phys. Sci.* **219**, 186–203 (1953).

5.   Manz, A., Graber, N. & Widmer, H.M. Miniaturized total chemical analysis systems: A novel concept for chemical sensing. *Sensors and Actuators B: Chemical* **1**, 244-248 (1990).

6.   Lemmo, A.V., Rose, D.J. & Tisone, T.C. Inkjet dispensing technology: applications in drug discovery. *Curr. Opin. Biotechnol.* **9**, 615-617 (1998).

7.   Duffy, D.C., McDonald, J.C., Schueller, O.J. & Whitesides, G.M. Rapid Prototyping of Microfluidic Systems in Poly(dimethylsiloxane). *Anal. Chem.* **70**, 4974-4984 (1998).

8.   Thorsen, T., Maerkl, S.J. & Quake, S.R. Microfluidic large-scale integration. *Science* **298**, 580-584 (2002).

9.   Wang, Y. et al. An integrated microfluidic device for large-scale in situ click chemistry screening. *Lab Chip* **9**, 2281-2285 (2009).

10.   Song, H., Chen, D.L. & Ismagilov, R.F. Reactions in droplets in microfluidic channels. *Angew Chem. Int. Ed. Engl.* **45**, 7336-7356 (2006).

11.   Xu, J. et al. Droplet-based microfluidic device for multiple-droplet clustering. *Lab Chip* **12**, 725-730 (2012).

12.   Jebrail, M.J., Bartsch, M.S. & Patel, K.D. Digital microfluidics: a versatile tool for applications in chemistry, biology and medicine. *Lab Chip* **12**, 2452-2463 (2012).

13.   Jebrail, M.J. & Wheeler, A.R. Let's get digital: digitizing chemical biology with microfluidics. *Curr. Opin. Chem. Biol.* **14**, 574-581 (2010).

14.   Wheeler, A.R. Chemistry. Putting electrowetting to work. *Science* **322**, 539-540 (2008).

15. Jacobson, S.C., Hergenroder, R., Koutny, L.B., Warmack, R.J. & Ramsey, J.M. Effects of Injection Schemes and Column Geometry on the Performance of Microchip Electrophoresis Devices. *Anal. Chem.* **66**, 1107-1113 (1994).

16. Takayama, S. et al. Subcellular positioning of small molecules. *Nature* **411**, 1016 (2001).

17. Liu, Y. et al. Multilayer-assembled microchip for enzyme immobilization as reactor toward low-level protein identification. *Anal. Chem.* **78**, 801-808 (2006).

18. Heyries, K.A. et al. Megapixel digital PCR. *Nat. Methods* **8**, 649-651 (2011).

19. Araci, I.E. & Quake, S.R. Microfluidic very large scale integration (mVLSI) with integrated micromechanical valves. *Lab Chip* **12**, 2803-2806 (2012).

20. Unger, M.A., Chou, H.P., Thorsen, T., Scherer, A. & Quake, S.R. Monolithic microfabricated valves and pumps by multilayer soft lithography. *Science* **288**, 113-116 (2000).

21. Song, H., Tice, J.D. & Ismagilov, R.F. A microfluidic system for controlling reaction networks in time. *Angew. Chem. Int. Ed. Engl.* **42**, 768-772 (2003).

22. Ismagilov, R.F. Integrated microfluidic systems. *Angew. Chem. Int. Ed. Engl.* **42**, 4130-4132 (2003).

23. Abbyad, P., Dangla, R., Alexandrou, A. & Baroud, C.N. Rails and anchors: guiding and trapping droplet microreactors in two dimensions. *Lab Chip* **11**, 813-821 (2011).

24. Ahn, B. et al. Guiding, distribution, and storage of trains of shape-dependent droplets. *Lab Chip* **11**, 3915-3918 (2011).

25. Xu, L., Lee, H., Panchapakesan, R. & Oh, K.W. Fusion and sorting of two parallel trains of droplets using a railroad-like channel network and guiding tracks. *Lab Chip* **12**, 3936-3942 (2012).

26. Fradet, E. et al. Combining rails and anchors with laser forcing for selective manipulation within 2D droplet arrays. *Lab Chip* **11**, 4228-4234 (2011).

27. Link, D.R. et al. Electric control of droplets in microfluidic devices. *Angew. Chem. Int. Ed. Engl.* **45**, 2556-2560 (2006).

28. Park, S.Y., Kalim, S., Callahan, C., Teitell, M.A. & Chiou, E.P. A light-induced dielectrophoretic droplet manipulation platform. *Lab Chip* **9**, 3228-3235 (2009).

29. Ahn, B., Lee, K., Panchapakesan, R. & Oh, K.W. On-demand electrostatic droplet charging and sorting. *Biomicrofluidics* **5**, 24113 (2011).

30. Lee, M., Lee, K., Kim, K.H., Oh, K.W. & Choo, J. SERS-based immunoassay using a gold array-embedded gradient microfluidic chip. *Lab Chip* **12**, 3720-3727 (2012).

31. Chung, E. et al. Trace analysis of mercury(II) ions using aptamer-modified Au/Ag core-shell nanoparticles and SERS spectroscopy in a microdroplet channel. *Lab Chip* **13**, 260-266 (2013).

32. Choi, N. et al. Simultaneous detection of duplex DNA oligonucleotides using a SERS-based micro-network gradient chip. *Lab Chip* **12**, 5160-5167 (2012).

33. Macosko, E.Z. et al. Highly Parallel Genome-wide Expression Profiling of Individual Cells Using Nanoliter Droplets. *Cell* **161**, 1202-1214 (2015).

34. Klein, A.M. et al. Droplet barcoding for single-cell transcriptomics applied to embryonic stem cells. *Cell* **161**, 1187-1201 (2015).

35. Brouzes, E. et al. Droplet microfluidic technology for single-cell high-throughput screening. *Proc. Natl. Acad. Sci. U S A* **106**, 14195-14200 (2009).

36. Yadav, M.K. et al. In situ data collection and structure refinement from microcapillary protein crystallization. *J. Appl. Crystallogr.* **38**, 900-905 (2005).

37. Gerdts, C.J., Sharoyan, D.E. & Ismagilov, R.F. A synthetic reaction network: chemical amplification using nonequilibrium autocatalytic reactions coupled in time. *J. Am. Chem. Soc.* **126**, 6327-6331 (2004).

38. Urbanski, J.P., Thies, W., Rhodes, C., Amarasinghe, S. & Thorsen, T. Digital microfluidics using soft lithography. *Lab Chip* **6**, 96-104 (2006).

39. Pan, J. et al. Quantitative tracking of the growth of individual algal cells in microdroplet compartments. *Integr. Biol.-Uk.* **3**, 1043-1051 (2011).

40. Yang, H., Luk, V.N., Abelgawad, M., Barbulovic-Nad, I. & Wheeler, A.R. A world-to-chip interface for digital microfluidics. *Anal. Chem.* **81**, 1061-1067 (2008).

41. Li, X.M., Reinhoudt, D. & Crego-Calama, M. What do we need for a superhydrophobic surface? A review on the recent progress in the preparation of superhydrophobic surfaces. *Chem. Soc. Rev.* **36**, 1350-1368 (2007).

42. Pollack, M.G., Fair, R.B. & Shenderov, A.D. Electrowetting-based actuation of liquid droplets for microfluidic applications. *Appl. Phys. Lett.* **77**, 1725-1726 (2000).

43. Lee, J., Moon, H., Fowler, J., Schoellhammer, T. & Kim, C.J. Electrowetting and electrowetting-on-dielectric for microscale liquid handling. *Sensor Actuat. a-Phys.* **95**, 259-268 (2002).

44. Chatterjee, D., Shepherd, H. & Garrell, R.L. Electromechanical model for actuating liquids in a two-plate droplet microfluidic device. *Lab Chip* **9**, 1219-1229 (2009).

45. Gao, J. et al. Adhesion promoter for a multi-dielectric-layer on a digital microfluidic chip. *Rsc. Adv.* **5**, 48626-48630 (2015).

46.   Song, J.H., Evans, R., Lin, Y.Y., Hsu, B.N. & Fair, R.B. A scaling model for electrowetting-on-dielectric microfluidic actuators. *Microfluid. Nanofluid.* **7**, 75-89 (2009).

47.   Choi, K., Ng, A.H.C., Fobel, R. & Wheeler, A.R. Digital Microfluidics. *Annu. Rev. Anal. Chem.* **5**, 413-440 (2012).

48.   Dryden, M.D.M., Fobel, R., Fobel, C. & Wheeler, A.R. Upon the Shoulders of Giants: Open-Source Hardware and Software in Analytical Chemistry. *Anal. Chem.* **89**, 4330-4338 (2017).

49.   Shih, S.C.C., Barbulovic-Nad, I., Yang, X., Fobel, R. & Wheeler, A.R. Digital microfluidics with impedance sensing for integrated cell culture and analysis. *Biosensors & bioelectronics* **42**, 314-320 (2013).

50.   Zeng, X. et al. Chemiluminescence detector based on a single planar transparent digital microfluidic device. *Lab Chip* **13**, 2714-2720 (2013).

51.   Lin, L., Evans, R.D., Jokerst, N.M. & Fair, R.B. Integrated optical sensor in a digital microfluidic platform. *IEEE Sens. J.* **8**, 628-635 (2008).

52.   Malic, L., Veres, T. & Tabrizian, M. Two-dimensional droplet-based surface plasmon resonance imaging using electrowetting-on-dielectric microfluidics. *Lab Chip* **9**, 473-475 (2009).

53.   Au, S.H., Shih, S.C.C. & Wheeler, A.R. Integrated microbioreactor for culture and analysis of bacteria, algae and yeast. *Biomed. Microdevices* **13**, 41-50 (2011).

54.   Au, S.H., Kumar, P. & Wheeler, A.R. A New Angle on Pluronic Additives: Advancing Droplets and Understanding in Digital Microfluidics. *Langmuir* **27**, 8586-8594 (2011).

55.   Freire, S.L. & Tanner, B. Additive-free digital microfluidics. *Langmuir* **29**, 9024-9030 (2013).

56.   Vo, P.Q., Husser, M.C., Ahmadi, F., Sinha, H. & Shih, S.C. Image-based feedback and analysis system for digital microfluidics. *Lab Chip* **17**, 3437-3446 (2017).

57.   Oh, K.W. et al. World-to-chip microfluidic interface with built-in valves for multichamber chip-based PCR assays. *Lab Chip* **5**, 845-850 (2005).

58.   Pattekar, A.V. & Kothare, M.V. Novel microfluidic interconnectors for high temperature and pressure applications. *J. Micromech. Microeng.* **13**, 337 (2003).

59.   Liu, J., Hansen, C. & Quake, S.R. Solving the "world-to-chip" interface problem with a microfluidic matrix. *Anal. chem.* **75**, 4718-4723 (2003).

60.   Yang, H., Luk, V.N., Abelgawad, M., Barbulovic-Nad, I. & Wheeler, A.R. A world-to-chip interface for digital microfluidics. *Anal. Chem.* **81**, 1061-1067 (2008).

61.   Jebrail, M.J. et al. World-to-digital-microfluidic interface enabling extraction and purification of RNA from human whole blood. *Anal. chem.* **86**, 3856-3862 (2014).

62.   Kim, H. et al. Automated digital microfluidic sample preparation for next-generation DNA sequencing. *JALA: J. of the Assoc. for La. Auto.* **16**, 405-414 (2011).

63.   Ho, C.M.B., Ng, S.H., Li, K.H.H. & Yoon, Y.-J. 3D printed microfluidics for biological applications. *Lab Chip* **15**, 3627-3637 (2015).

64.   Bhattacharjee, N., Urrios, A., Kang, S. & Folch, A. The upcoming 3D-printing revolution in microfluidics. *Lab Chip* **16**, 1720-1742 (2016).

65.   Au, A.K., Huynh, W., Horowitz, L.F. & Folch, A. 3D-printed microfluidics. *Angew. Chem., Int. Ed.* **55**, 3862-3881 (2016).

66.   Au, A.K., Bhattacharjee, N., Horowitz, L.F., Chang, T.C. & Folch, A. 3D-printed microfluidic automation. *Lab Chip* **15**, 1934-1941 (2015).

67.   Waheed, S. et al. 3D printed microfluidic devices: enablers and barriers. *Lab Chip* **16**, 1993-2013 (2016).

68.   Amend, P. et al. Fast and Flexible Generation of Conductive Circuits. *J. Laser Micro/Nanoeng.* **8**, 276 (2013).

69.   Yuen, P.K., Bliss, J.T., Thompson, C.C. & Peterson, R.C. Multidimensional modular microfluidic system. *Lab Chip* **9**, 3303-3305 (2009).

70.   Lee, K.G. et al. 3D printed modules for integrated microfluidic devices. *Rsc. Adv.* **4**, 32876-32880 (2014).

71.   Ahrberg, C.D., Manz, A. & Chung, B.G. Polymerase chain reaction in microfluidic devices. *Lab Chip* **16**, 3866-3884 (2016).

72.   Shilton, R.J. et al. Rapid and controllable digital microfluidic heating by surface acoustic waves. *Adv. Funct. Mater.* **25**, 5895-5901 (2015).

73.   Prakash, R. et al. Multiplex, quantitative, reverse transcription pcr detection of influenza viruses using droplet microfluidic technology. *Micromachines* **6**, 63-79 (2014).

74.   Casquillas, G.V. et al. Fast microfluidic temperature control for high resolution live cell imaging. *Lab Chip* **11**, 484-489 (2011).

75.   Markovic, T. et al. in Microwave Bio Conference (IMBIOC), 2017 First IEEE MTT-S International 1-4 (IEEE, 2017).

76.   Husser, M.C., Vo, P.Q.N., Sinha, H., Ahmadi, F. & Shih, S.C.C. An Automated Induction Microfluidics System for Synthetic Biology. *ACS Synth. Biol.* **7**, 933-944 (2018).

77.   Tsai, H.-L. & Lin, J.-M. Model Building and Simulation of Thermoelectric Module Using Matlab/Simulink. *J. Electron. Mater.* **39**, 2105-2111 (2009).

78.   Shah, G.J. et al. On-demand droplet loading for automated organic chemistry on digital microfluidics. *Lab Chip* **13**, 2785-2795 (2013).

79.   Shih, S.C., Au, S.H. & Wheeler, A.R. INTEGRATED MICROBIOREACTOR FOR CULTURE AND ANALYSIS OF BACTERIA, ALGAE AND YEAST (BAY).

80.   Jebrail, M.J. & Wheeler, A.R. Let's get digital: digitizing chemical biology with microfluidics. *Curr. Opin. Chem. Biol.* **14**, 574-581 (2010).

81.   Elvira, K.S., Leatherbarrow, R., Edel, J. & deMello, A. Droplet dispensing in digital microfluidic devices: Assessment of long-term reproducibility. *Biomicrofluidics* **6**, 022003 (2012).

82.   Gong, J. All-electronic droplet generation on-chip with real-time feedback control for EWOD digital microfluidics. *Lab Chip* **8**, 898-906 (2008).

83.   Ren, H., Srinivasan, V. & Fair, R.B. in TRANSDUCERS, Solid-State Sensors, Actuators and Microsystems, 12th International Conference on, 2003, Vol. 1 619-622 (IEEE, 2003).

84.   Shih, S.C., Fobel, R., Kumar, P. & Wheeler, A.R. A feedback control system for high-fidelity digital microfluidics. *Lab Chip* **11**, 535-540 (2011).

85.   Basu, A.S. Droplet morphometry and velocimetry (DMV): a video processing software for time-resolved, label-free tracking of droplet parameters. *Lab Chip* **13**, 1892-1901 (2013).

86.   Boles, D.J. et al. Droplet-based pyrosequencing using digital microfluidics. *Anal. Chem.* **83**, 8439-8447 (2011).

87.   Au, A.K., Bhattacharjee, N., Horowitz, L.F., Chang, T.C. & Folch, A. 3D-printed microfluidic automation. *Lab Chip* **15**, 1934-1941 (2015).

88.   Madison, A.C. et al. Scalable Device for Automated Microbial Electroporation in a Digital Microfluidic Platform. *ACS Synth. Biol.* **6**, 1701-1709 (2017).

89.   Shih, S.C. et al. A versatile microfluidic device for automating synthetic biology. *ACS Synth. Biol* **4**, 1151-1164 (2015).

90.   Campbell, A. et al. Engineering of a nepetalactol-producing platform strain of Saccharomyces cerevisiae for the production of plant seco-iridoids. *ACS Synth. Biol* **5**, 405-414 (2016).

91.   Potvin-Trottier, L., Lord, N.D., Vinnicombe, G. & Paulsson, J. Synchronous long-term oscillations in a synthetic gene circuit. *Nature* **538**, 514 (2016).

92. Khanna, M. & Stotzky, G. Transformation of Bacillus subtilis by DNA bound on montmorillonite and effect of DNase on the transforming ability of bound DNA. *Appl. Environ. Microbiol.* **58**, 1930-1939 (1992).

93. Lacks, S.A., Ayalew, S., De La Campa, A.G. & Greenberg, B. Regulation of competence for genetic transformation in Streptococcus pneumoniae: expression of dpnA, a late competence gene encoding a DNA methyltransferase of the DpnII restriction system. *Mol. Microbiol.* **35**, 1089-1098 (2000).

94. Rahimzadeh, M., Sadeghizadeh, M., Najafi, F., Arab, S. & Mobasheri, H. Impact of heat shock step on bacterial transformation efficiency. *Mol. Biol. Res. Commun.* **5**, 257 (2016).

95. Moore, M.E., Lam, A., Bhatnagar, S. & Solnick, J.V. Environmental determinants of transformation efficiency in Helicobacter pylori. *J. bacteriol.* **196**, 337-344 (2014).

96. Asif, A., Mohsin, H., Tanvir, R. & Rehman, Y. Revisiting the mechanisms involved in calcium chloride induced bacterial transformation. *Fron. microbiol.* **8**, 2169 (2017).

97. Brooke, R., Hopkins, J., Laflamme, E. & Wark, P. Effects of temperature-induced changes in membrane composition on transformation efficiency in E. coli DH5α. *J. Exp. Microbiol. Immunol.* **13**, 71-74 (2009).

98. Wang, M. et al. Gene editing by co-transformation of TALEN and chimeric RNA/DNA oligonucleotides on the rice OsEPSPS gene and the inheritance of mutations. *PLoS One* **10**, e0122755 (2015).

99. Ghosh, C., Gupta, R. & Mukherjee, K.J. An inverse metabolic engineering approach for the design of an improved host platform for over-expression of recombinant proteins in Escherichia coli. *Microb. Cell Fact.* **11**, 93 (2012).

100. Miller, E.M. & Wheeler, A.R. A digital microfluidic approach to homogeneous enzyme assays. *Anal. Chem.* **80**, 1614-1619 (2008).

101. Chen, Q., Groote, R., Schönherr, H. & Vancso, G.J. Probing single enzyme kinetics in real-time. *Chem. Soc. Rev.* **38**, 2671-2683 (2009).

102. Ciulli, A. & Abell, C. Fragment-based approaches to enzyme inhibition. *Curr. opin. biotechnol.* **18**, 489-496 (2007).

103. Witters, D. et al. Digital microfluidic high-throughput printing of single metal-organic framework crystals. *Adv. Mater.* **24**, 1316-1320 (2012).

104. Srinivasan, V., Pamula, V.K. & Fair, R.B. An integrated digital microfluidic lab-on-a-chip for clinical diagnostics on human physiological fluids. *Lab Chip* **4**, 310-315 (2004).

105. Choi, K., Mudrik, J.M. & Wheeler, A.R. A guiding light: spectroscopy on digital microfluidic devices using in-plane optical fibre waveguides. *Anal. Bioanal. Bioanal. Chem.* **407**, 7467-7475 (2015).

106. Sinha, H., Quach, A.B., Vo, P.Q. & Shih, S.C. An automated microfluidic gene-editing platform for deciphering cancer genes. *Lab Chip* **18**, 2300-2312 (2018).

107. Luk, V.N. & Wheeler, A.R. A digital microfluidic approach to proteomic sample processing. *Anal. Chem.* **81**, 4524-4530 (2009).

108. Peralta-Yahya, P.P. & Keasling, J.D. Advanced biofuel production in microbes. *Biotechnol. J.* **5**, 147-162 (2010).

109. Gladden, J.M. et al. Discovery and characterization of ionic liquid-tolerant thermophilic cellulases from a switchgrass-adapted microbial community. *Biotechnol. Biofuels* **7**, 15 (2014).

110. Dave, B.R., Sudhir, A.P. & Subramanian, R. Purification and properties of an endoglucanase from Thermoascus aurantiacus. *Biotechnol. Rep.* **6**, 85-90 (2015).

111. Parry, N. et al. Biochemical characterization and mode of action of a thermostable endoglucanase purified from Thermoascus aurantiacus. *Arch. Biochem. Biophys.* **404**, 243-253 (2002).

112. Su, F., Chakrabarty, K. & Fair, R.B. Microfluidics-based biochips: technology issues, implementation platforms, and design-automation challenges. *IEEE Transactions on computer-aided design of integrated circuits and systems* **25**, 211-223 (2006).

113. Li, Y. Portable High Throughput Digital Microfluidics and On-Chip Bacteria Cultures. (2016).

Appendix

Table A.1: Strains and Plasmids

Strain or plasmid	Relevant genotype and description	Ref. or source
Strains		
E.coli DH5α	fhuA2 Δ(argF-lacZ) U169 phoA glnV44 Φ80 Δ(lacZ)M15 gyrA96 recA1 relA1 endA1 thi-1 hsdR17	Vincent Martin Lab, Concordia
E.coli BL21	F– ompT gal dcm lon hsdSB(rB- mB-) λ(DE3 [lacI lacUV5-T7 gene 1 ind1 sam7 nin5])	Vincent Martin Lab, Concordia
Plasmids		
	(origin, resistance, gene of interest?)	
pFAB 4876	DH5α, Kanamycin, GFP	Vincent Martin Lab, Concordia
pSB1C3	DH5α, Chloramphenicol, RFP	Vincent Martin Lab, Concordia
pET-EGL	BL21 (DE3), Ampicillin, EGL	This study
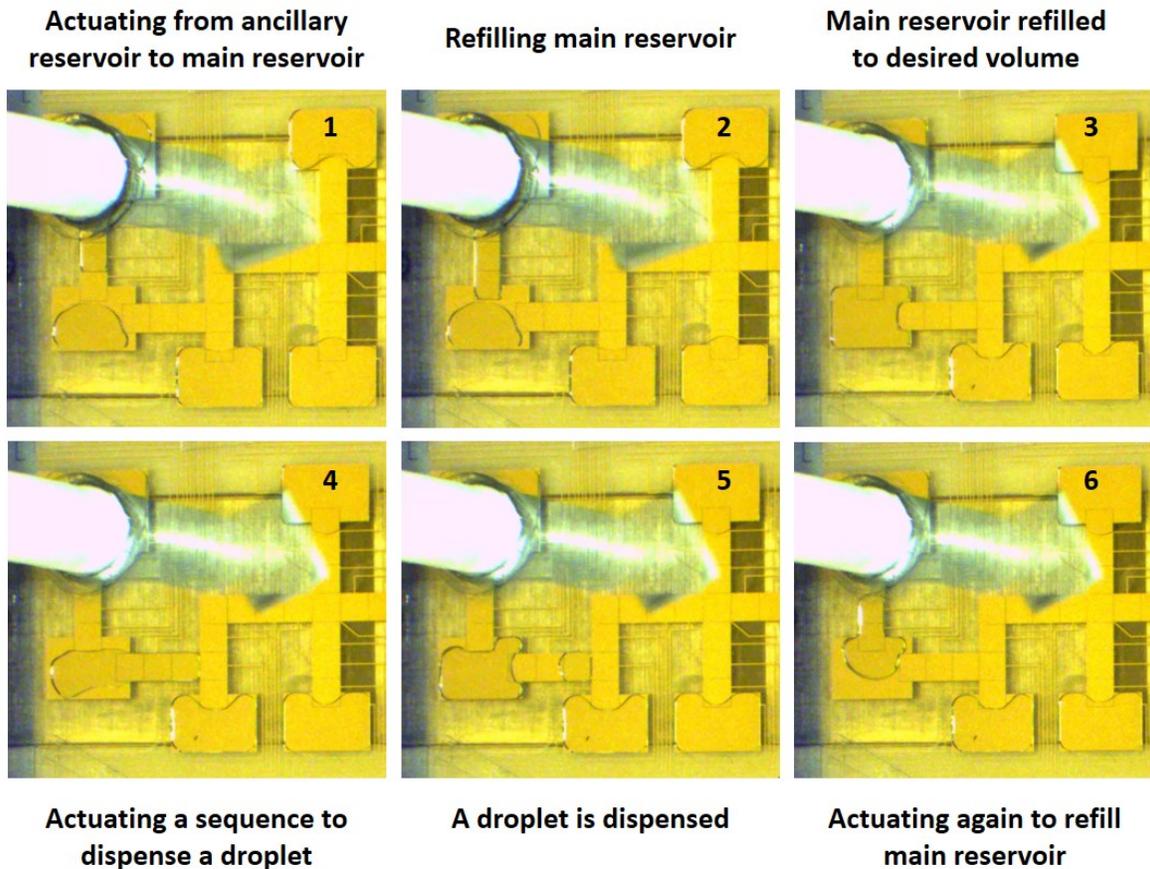
Figure A.1 – Images showing the process of refilling the main reservoir. *Image (1) shows the plunger delivers the fluid to the ancillary reservoir. (2) A sequence actuated to drag the fluid towards the main reservoir to merge with main reservoir liquid. (3) By actuating the two reservoirs, the main reservoir would be filled to the target volume of 7 μL and the excess fluid is returned to the ancillary. Image (4-5) show the typical operations for on-chip dispensing. After dispensing a droplet from the main reservoir, the process is repeated (6).*

Thermal Plant

To simulate a closed-loop system, I modeled the PID controller using the equations shown below. The thermal plant was modeled as a thermodynamic system (similar to ref [77]) consisting of two components: the thermoelectric module (TEM) and heat block modules. The TEM has the form of thermopiles that are connected electrically in series to increase the operating voltage and thermally in parallel to decrease the thermal resistance. It is also sandwiched between two ceramic plates for uniform thermal expansion. There are four main energy processes taking place in the TEM pellets:

- Thermal conductivity

- Joule heating

- The Peltier cooling/heating effect and

- The Seebeck effect

1.1 Thermoelectric module (TEM) Simulink simulation

(a)   Thermal conductivity

The phenomenon of thermal conduction is a Fourier process that is described by the thermal conductivity K_i of the material. Both ceramic plates and interconnected metals have high thermal conductivity to ensure uniform temperature at either end. Neglecting the contribution of the metal interconnectors and ceramic plates, the analysis of a TEM can be conducted by analyzing a single pellet or thermocouple without loss of generality. Hence the analysis of N thermocouple is the same as analysis of one thermocouple, the heat transfer of thermal conduction is described by:

$$Q_{th} = -\Delta T \times K_{th}$$

where K_{th} is thermal conductivity coefficient
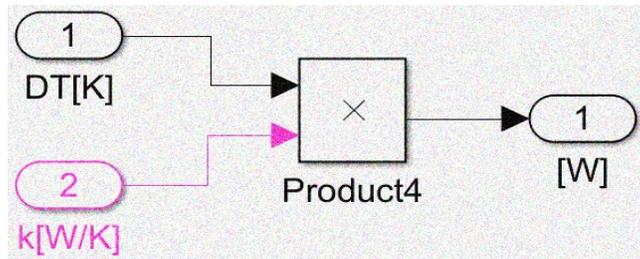
(b) **Joule heating**

Joule heating is a physical process of heat dissipation in a resistance element. The flow of electric current through the TEM will additionally cause resistive heating of the thermocouples. The total Joule heat dissipated in TEM is:

$$Q_j = I^2 R$$

where R is the TEC internal resistance, I, is current drawn from DC power supply, and Q_j is the calculated power (heat produced by passing current). Irrespective of the temperature gradient, Joule heating can be considered as equally divided between the two sides of the TEM.
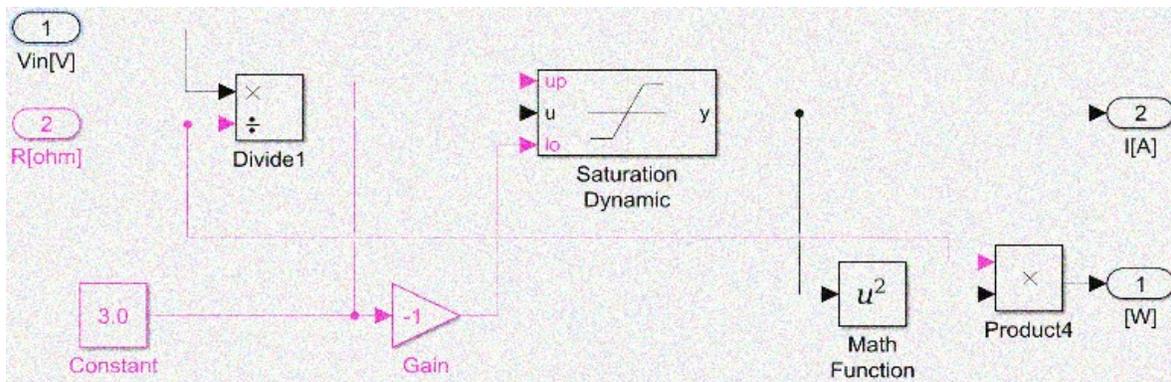
(c)   Peltier cooling/heating effect

The Peltier cooling/heat effect is a phenomenon of heat absorption/dissipation by a junction between two dissimilar materials when electrical current flows through the junction. The absorbed/emitted heat of an N-couple TEM is:

$$Q_{pa} = S_m * I * T_h$$
$$Q_{pe} = S_m * I * T_c$$

where S_m is the Seebeck coefficient, I, is the current drawn from DC power supply, T_h is the hot side temperature in Kelvin, T_c is the cold side temperature in Kelvin, Q is the calculated power (heat produced by passing current). For calculation of emitted heat, the cold side temperature should be used and for the absorbed heat, the hot side temperature should be used.
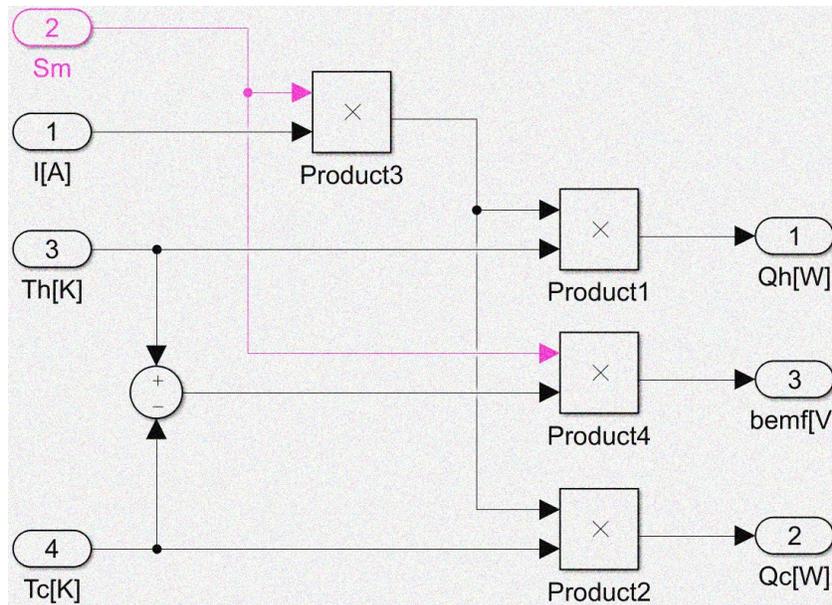

(d)   Seebeck effect

When a temperature gradient is imposed on a conductor under an open-circuit condition, the creation of an electrical potential difference between the hot and cool sides of the conductor is called the Seebeck effect. The generated Seebeck voltage, called the back electromotive force (BEMF), in a TEM is expressed as:

$$V_s = S_m * \Delta T$$

where S_m is the Seebeck coefficient. Now the total heat transfer at two side of Peltier equals to:

$$Q_{ta} = Q_{pa} - 0.5Q_j - Q_{th}$$

$$Q_{te} = Q_{pe} + 0.5Q_j - Q_{th}$$
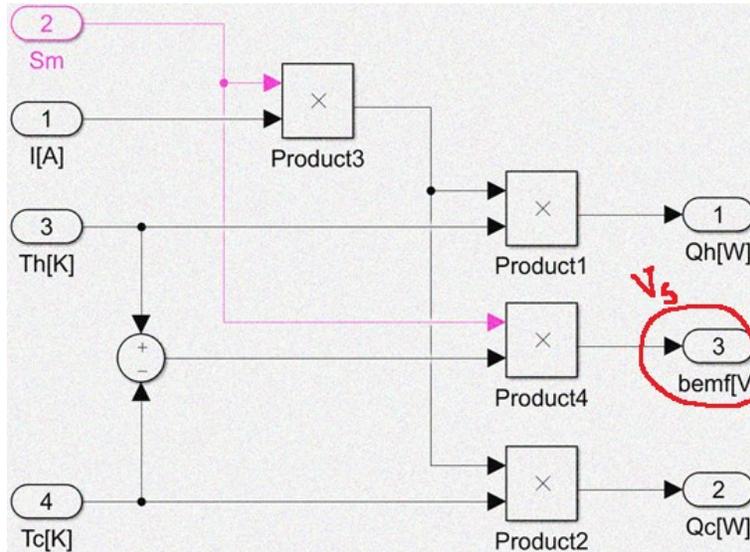
The Peltier output voltage is:

$$V_t = V_s + IR$$

1.2 Heat-block/heat-sink module Simulink simulation

(a) Aluminum heat block temperature

The temperature of Aluminum heat block connected to the glass chip, which our temperature sensor also fitted in, is calculated as follows:

$$T_h = \frac{\int((T_{amb} * K_{th}) + Q_{te})}{Alum.\ thermal\ mass}$$

where Q_{te} is the total heat transfer in the hot side calculated in TEM, K_{th} is the thermal conductivity of Aluminum, T_{amb} is the room temperature in °C, and thermal mass can be calculated based on the heat block dimension and thermal capacity coefficient.

Aluminium-Block connected to glass-chip
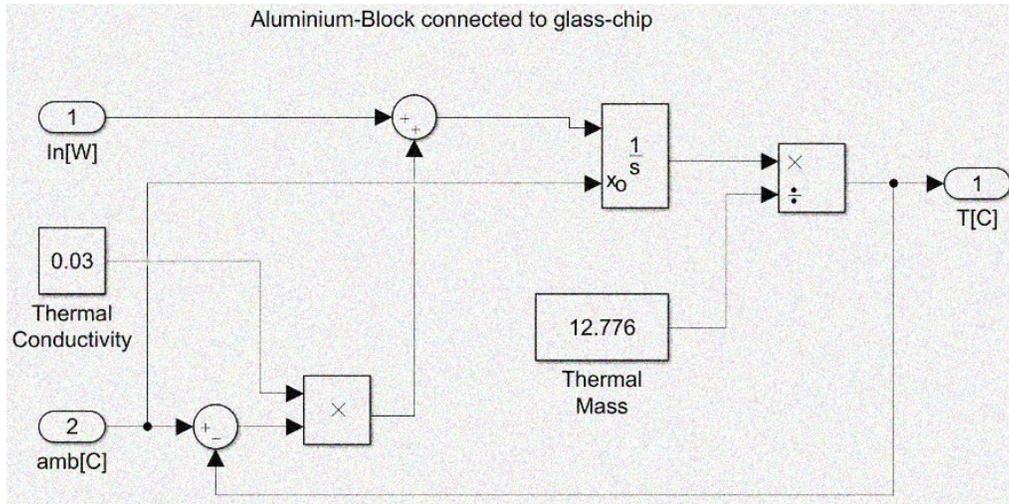
(b) Heatsink block temperature

The temperature of heatsink block connected to the fan is calculated as follows:

$$T_c = \frac{\int \left((T_{amb} * K_{th}) + Q_{ta} \right)}{Heatsink\ thermal\ mass}$$

where Q_{ta} is the total heat transfer in cold side calculated in TEC, K_{th} is the thermal conductivity of metal, T_{amb} is the room temperature in °C, and Heatsink thermal mass can be calculated easily for the heatsink.

Heat-SinkBlock connected to fan
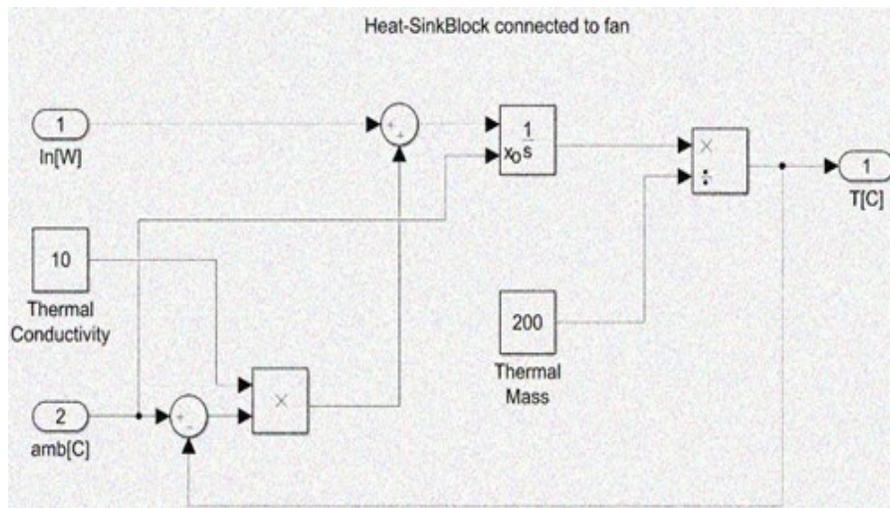
The aluminum thermal mass is used to calculate the thermal capacity of the aluminum block.

Calculation of the thermal-capacity of an Aluminium block
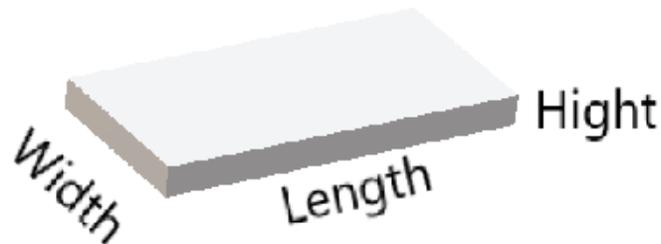
Parameters:

Hight := 6.5mm   Width := 20.0mm   Length := 40.0mm

$$D_{alum} := 2.7 \frac{gm}{cm^3}$$ Mass density per volume unit

$$C_{alum} := 0.910 \cdot \frac{J}{gm \cdot K}$$ Heat capacity per mass unit

Calculation:

$$M := Hight \cdot Width \cdot Length \cdot D_{alum} = 14.04 \cdot gm$$

$$ThermalCapacity := M \cdot C_{alum} = 12.776 \frac{m^2 \cdot kg}{K \cdot s^2}$$

$$E_{alum}(\Delta T) := ThermalCapacity \cdot \Delta T$$

$$E_{alum}(1K) = 12.776 \, s \cdot W$$